

저석 있음: 번호 매기기: 구역마다 다시 매기기

# 1 Integration of GOCI and AHI Yonsei Aerosol Optical Depth 2 Products During the 2016 KORUS-AQ and 2018 EMeRGe 3 Campaigns

4  
5 Hyunkwang Lim<sup>1</sup>, Sujung Go<sup>1,2</sup>, Jhoon Kim<sup>1</sup>, Myungje Choi<sup>2,3</sup>, Seoyoung Lee<sup>1</sup>, Chang-Keun Song<sup>4</sup>, Yasuko  
6 Kasai<sup>5</sup>

7 <sup>1</sup>Department of Atmospheric Sciences, Yonsei University, Seoul 03722, Republic of Korea

8 <sup>2</sup>Joint Center for Earth Systems Technology, University of Maryland Baltimore County, Baltimore, MD, USA

9 <sup>3</sup>Jet Propulsion Laboratory, California Institute of Technology, Pasadena, CA, USA

10 <sup>4</sup>School of Urban and Environmental Engineering, Ulsan National Institute of Science and Technology, Ulsan  
11 44919, Republic of Korea

12 <sup>5</sup>Natinal Institute of Information and Communications Technology, Tokyo 184-8759, Japan

13  
14  
15 *Correspondence to:* Jhoon Kim (jkim2@yonsei.ac.kr)

16 **Abstract.** The Yonsei AEROSOL Retrieval (YAER) algorithm for the Geostationary Ocean  
17 Color Imager (GOCI) retrieves aerosol optical properties only over dark surfaces, so it is  
18 important to mask pixels with bright surfaces. The Advanced Himawari Imager (AHI) is  
19 equipped with three shortwave-infrared and nine infrared channels, which is advantageous for  
20 bright-pixel masking. In addition, multiple visible and near-infrared channels provide a great  
21 advantage in aerosol property retrieval from the AHI and GOCI. By applying the YAER  
22 algorithm to 10 minute AHI or 1 hour GOCI data at 6 km × 6 km resolution, diurnal  
23 variations and aerosol transport can be observed, which has not previously been possible  
24 from low-earth-orbit satellites. This study attempted to estimate the optimal aerosol optical  
25 depth (AOD) for East Asia by data fusion, taking into account satellite retrieval uncertainty.  
26 The data fusion involved two steps: (1) analysis of error characteristics of each retrieved  
27 result with respect to the ground-based Aerosol Robotic Network (AERONET), and bias  
28 correction based on normalized difference vegetation indexes; and (2) compilation of the  
29 fused product using ensemble-mean and maximum-likelihood estimation methods (MLE).  
30 Fused results show a better statistics in terms of fraction within the expected error, correlation  
31 coefficient, root-mean-square error, median bias error than the retrieved result for each  
32 product. [If the root mean square error and Gaussian center values used for MLE fusion are correct, the MLE fused products show better accuracy, but the ensemble-mean products can still be used as useful as MLE.](#)

저석 지정함: 글꼴: (한글) 바탕

## 35 1. Introduction

36 Aerosols are generated by human activities and natural processes on local to global scales,  
37 and have a lifetime of several to tens of days. Aerosols affect Earth's radiative energy balance  
38 by scattering and absorption (e.g. Cho et al., 2003). High aerosol loadings are persistent in  
39 Northeast Asia, including diverse aerosol types from various sources. Interactions among  
40 aerosols, clouds, and radiation in the atmosphere cause significant uncertainties in climate-  
41 model calculations (IPCC, 2013). Datasets produced by satellites have been widely used to  
42 reduce such uncertainties (Saide et al., 2014; Pang et al., 2018), but the systems must be

43 accurately calibrated, verified, and consistent. Satellite data have been used extensively to  
44 retrieve aerosol optical properties (AOPs) over broad areas, with several algorithms having  
45 been developed. Satellites in low earth orbit (LEO), including Sun-synchronous orbit (SSO),  
46 cover the entire Earth over one to several days, depending on instrument and orbit  
47 characteristics. Most aerosol retrieval algorithms have been developed for LEO satellites  
48 (Kim et al., 2007; Lyapustin et al., 2011a, b; Lee et al., 2012; Fukuda et al., 2013; Hsu et al.,  
49 2013; Levy et al., 2013; Garay et al., 2017, 2020). LEO instruments currently onboard  
50 satellites include the Moderate Resolution Imaging Spectrometer (MODIS), Visible Infrared  
51 Imaging Radiometer Suite (VIIRS), Multi-angle Imaging SpectroRadiometer (MISR), and  
52 Cloud and Aerosol Imager (CAI) (Remer et al., 2005; Lyapustin et al., 2011a, b, 2018;  
53 Fukuda et al., 2013; Hsu et al., 2013; Levy et al., 2013; Garay et al., 2017, 2020; [Jackson et](#)  
54 [al., 2013](#); Lee et al., 2017).

55 Representative algorithms developed for MODIS data include the Dark-Target (DT; Remer  
56 et al., 2005; Levy et al., 2013), Deep Blue (DB; Hsu et al., 2013; Sayer et al., 2014), and  
57 Multi-Angle Implementation of Atmospheric Correction (MAIAC; Lyapustin et al., 2011a, b)  
58 systems, which are also applied for the succeeding VIIRS (Sayer et al., 2018). In the DT  
59 algorithm, the 2.1  $\mu\text{m}$  channel is used to estimate land-surface reflectance in the visible (VIS)  
60 region using empirical equations based on the normalized difference vegetation index  
61 (NDVI). The DT algorithm has improved surface-reflectance modelling through  
62 consideration of the fractional area of urbanization (Gupta et al., 2016). Ocean-surface  
63 reflectance is estimated using the Cox and Munk method (Cox and Munk, 1954), and AOPs  
64 over land and ocean are provided at spatial resolutions of  $10 \text{ km} \times 10 \text{ km}$  and  $3 \text{ km} \times 3 \text{ km}$   
65 (Remer et al., 2013), respectively. The DB algorithm has an advantage over the DT algorithm  
66 in allowing aerosol data retrieval over bright surfaces. By using a shorter-wavelength channel,  
67 accuracy is improved over bright surfaces such as urban and desert areas, where surface  
68 reflectance was previously estimated by the minimum reflectance method (MRM; Herman  
69 and Celarier 1997; Koelemeijer et al., 2003; Hsu et al., 2004). Furthermore, with the  
70 improvement to Collection 6.1, land-surface reflectance can be estimated similarly to the DT  
71 method, over densely vegetated regions (Sayer et al., 2019). In the case of VIIRS DB, aerosol  
72 retrieval over the ocean is also applied by the Satellite Ocean Aerosol Retrieval (SOAR)  
73 algorithm (Sayer et al., 2018). In the MODIS MAIAC system, surface reflectance is  
74 estimated by considering various images based on time-series analysis, with multi-angle  
75 observations, based on up to 16 day data, and by applying the bidirectional reflectance  
76 distribution function (BRDF). Ocean-surface reflectance is determined using a Cox and  
77 Munk BRDF model similar to DT and VIIRS DB (Lyapustin et al., 2011a, b, 2018). The  
78 MISR observes Earth at nine different angles, providing a high degree of freedom **for signals**;  
79 consequently, retrievals yield estimates of aerosol type and shape. As with the MAIAC,  
80 multiple observations are used, with the estimation of land-surface reflectance involving  
81 bidirectional reflectance factors (BRF). Zhang et al. (2016) developed an aerosol retrieval  
82 algorithm that allows aerosol data retrieval over bright land surfaces using surface-reflectance  
83 ratios from the VIIRS.

84 Aerosol retrieval algorithms for geosynchronous Earth orbit (GEO) satellites have been  
85 developed, including the Geostationary Operational Environmental Satellite (GOES) series in  
86 the USA (Knapp et al., 2005), Meteosat series in Europe (Bernard et al., 2011), Himawari  
87 series in Japan (Yoon et al., 2007; Kim et al., 2008; Lim et al., 2018; Kikuchi et al., 2018;  
88 Yoshida et al., 2018; Gupta et al., 2019), and the Geostationary Korea Multi-Purpose Satellite  
89 (GEO-KOMPSAT, GK) series in South Korea (Kim et al., 2014, 2016; Choi et al., 2016,  
90 2018; Kim et al., 2020). However, previously launched geostationary meteorological  
91 satellites had only a single, broadband VIS channel, with which it is difficult to retrieve

서식 지정함: 글꼴: (한글) 바탕, (한글) 한국어

삭제함: in

93 AOPs other than aerosol optical depth (AOD) (Wang et al., 2003; Knapp et al., 2005; Kim et  
 94 al., 2008, 2014, 2016; Bernard et al., 2011). However, the Geostationary Ocean Color Imager  
 95 (GOCI) onboard the GK-1 satellite, also known as the Communication, Ocean, and  
 96 Meteorological Satellite (COMS), has six VIS and two near-infrared (NIR) channels, which  
 97 is advantageous for retrieving AOPs (Lee et al., 2010; Choi et al., 2016, 2018; Kim et al.,  
 98 2017). Next-generation meteorological GEO satellite instruments, including the Advanced  
 99 Himawari Imager (AHI), Advanced Baseline Imager (ABI), and Advanced Meteorological  
 100 Imager (AMI), have three to four VIS and NIR channels, which enable aerosol property  
 101 retrieval with high accuracy (Lim et al., 2016, 2018; Kikuchi et al., 2018; Yoshida et al.,  
 102 2018; Gupta et al., 2019). Kikuchi et al. (2018) and Yoshida et al. (2018) performed aerosol  
 103 retrievals using the MRM and corrected reflectance using empirical equations. Gupta et al.  
 104 (2019) extended the MODIS DT algorithm to GEO satellites and estimated visible surface  
 105 reflectance using SWIR reflectance. Lim et al. (2018) retrieved the AOPs using both MRM  
 106 and estimated surface reflectance from short-wave IR (SWIR) data (ESR), and presented the  
 107 two merged products: an L2-AOD merged product, and a reprocessed AOD produced by  
 108 merging MRM and ESR surface reflectances. The MRM gives better accuracy over brighter  
 109 surfaces such as urban areas, while the ESR method gives better accuracy over areas of dense  
 110 vegetation (Lim et al., 2018). However, there is a critical surface reflectance at which aerosol  
 111 signals disappear, depending on the single-scattering albedo (Kim et al., 2016). Over the  
 112 ocean, both the MRM and ESR methods give high accuracy, but ESR results are robust with  
 113 the Cox and Munk model.  
 114 The MRM requires more computational time than the ESR method to estimate surface  
 115 reflectance, as it requires data for the past 30 days, and LER needs to be calculated using a  
 116 radiative transfer model. The ESR method estimates surface reflectance from the observed  
 117 TOA reflectance at 1.6  $\mu\text{m}$  wavelength using empirical equations including the NDVI. The  
 118 advantage of MRM is that stable surface reflectance values can be obtained regardless of  
 119 surface type. However, due to the influence of background aerosol optical depth (BAOD),  
 120 surface reflectance tends to be overestimated, with satellite-derived AOD data thus being  
 121 underestimated (Kim et al., 2014). On the other hand, the ESR method uses TOA reflectance  
 122 at 1.6  $\mu\text{m}$  wavelength to detect surface signals, which is less sensitive to fine particles and  
 123 BAOD. However, when aerosols such as yellow dust with coarse particles are transported  
 124 from the Taklamakan and Gobi deserts, the BAOD effect also applies to the ESR method.  
 125 The ESR method is also more likely to be affected by snow surfaces than the MRM, as snow  
 126 reduces reflectivity around the 1.6  $\mu\text{m}$  wavelength (Negi and Kokhanovsky, 2011). The ESR  
 127 method also has the disadvantage of giving noisy results over bright surfaces such as desert.  
 128 However, its fast surface-reflectance estimation enables near-real-time retrieval based on the  
 129 AHI YAER algorithm.

약제함: estimated surface reflectance,

[4] 이동함(삽입)

서식 지정함: 글꼴: (한글) 바탕, (한글) 한국어

130 <sup>▲</sup>  
 131 Algorithms developed to date for LEO and GEO satellites have both advantages and  
 132 disadvantages, depending on algorithm characteristics. Therefore, the MODIS team provides  
 133 combined DT and DB AOD products (Levy et al., 2013; Sayer et al., 2014). In addition,  
 134 several studies of the fusion of L2 products have been conducted (Levy et al., 2013; Sayer et  
 135 al., 2014; Wei et al., 2019), with Bilal et al. (2017) obtaining reliable results from merged DT  
 136 and DB products, as indicated by the NDVI in East Asia, and also robust products by simply  
 137 averaging DT and DB without consideration of the NDVI.  
 138 AOP data fusion in East Asia may also be achieved using aerosol products of AMI, GOCI-2,  
 139 and the geostationary environment monitoring spectrometer (GEMS) onboard the GK-2A and  
 140 2B satellites launched by South Korea in 2018 and 2020, respectively, with accuracy over  
 141 bright surfaces being improved by the GEMS aerosol product. It is also possible to obtain

143 accurate AOPs, such as single-scattering albedo, aerosol loading height, and fine-mode  
 144 fraction, which have been difficult to obtain by fusion of L2 data and/or surface reflectance  
 145 data. If the trace-gas dataset retrieved from GEMS is used, it is possible to improve the  
 146 aerosol type, with the retrieval of high-quality AOD data (Go et al., 2020).  
 147 Several studies have considered AOD data fusion, for which methods can be broadly  
 148 classified into two types. First, the fusion of more than one AOD product may involve  
 149 optimal interpolation (Xue et al., 2012), linear or second-order polynomial functions (Mélin  
 150 et al., 2007), arithmetic or weighted means (Gupta et al., 2008), or maximum-likelihood  
 151 estimates (MLE) (Nirala, 2008; Xu et al., 2015; Xie et al., 2018). Second, in the absence of  
 152 satellite-derived AOD products for the day of fusion, the geostatistical fusion method,  
 153 universal kriging method (Chatterjee et al., 2010; Li et al., 2014), geostatistical inverse  
 154 modelling (Wang et al., 2013), or spatial statistical data fusion (Nguyen et al., 2012) may be  
 155 applied. These have the advantage that AOD can be estimated by integrating the spatial  
 156 autocorrelation of AOD data even for pixels missing from the AOD products, although there  
 157 is a disadvantage in not considering temporal correlations. The Bayesian maximum entropy  
 158 (BME) method, taking into account temporal autocorrelation, has also been developed (Tang  
 159 et al., 2016). BME methodology can estimate gap-filling pixels that are difficult to retrieve  
 160 due to clouds, but with somewhat reduced accuracy. Gap filled AOD using the BME method,  
 161 and satellite-derived AOD discontinuity arises from insufficient temporal sampling being  
 162 available with the use of LEO satellites, resulting in a low fusion synergy. Previous studies  
 163 mentioned above include data fusion based on Kriging, reproduction of spectral AOD, and  
 164 BME method. Most of them focus on gap filling and rebuild AOD in areas not observed by  
 165 MISR, MODIS, and SeaWiFS, and so on (Wang et al., 2013; Tang et al., 2016). However in  
 166 this study, we focused on optimized AOD products with improved accuracy at the retrieved  
 167 pixels by ensemble-mean and MLE fusion. We compared these two products, one very  
 168 simple one and the other with more elaborated processes. As previous AOD fusion studies  
 169 improved the retrieved results mainly based on MLE or NDVI-based fusion studies (Bilal et  
 170 al., 2017; Levy et al., 2013; Wei et al., 2019; Go et al., 2020), we tried to further improve  
 171 them with efficient approach to save computation time considering the nature of satellite data  
 172 file size and user's near-real-time demand for data assimilation.  
 173 In this study, the GEO satellite dataset was used to resolve the temporal sampling issue for  
 174 data fusion, while maintaining the spatio-temporal resolution retrieved from GEO satellites.  
 175 We also attempted to estimate fused AOD products at 550nm with higher accuracy in East  
 176 Asia. The ensemble-mean and MLE methods were applied. Section 2 describes the two  
 177 algorithms used in this study for AHI and GOCI. Section 3 mentions methods of fusion and  
 178 systematic bias correction, and section 4 performs validation of the fused products with the  
 179 Aerosol Robotic Network (AERONET) instruments during two field campaigns: the Korea–  
 180 United States Air Quality Study (KORUS-AQ) and the Effect of Megacities on the Transport  
 181 and Transformation of Pollutants on Regional and Global Scales Study (EMeRGe).

약제함:

## 182 2. Descriptions of AHI, GOCI, the YAER algorithm.

약제함: , and the two field campaigns

### 183 2.1 AHI aerosol algorithm

184 The Himawari-8 and -9 satellites were launched by the Japanese Meteorological Agency  
 185 (JMA) on 7 October 2014 and 2 November 2016, respectively. The AHI onboard these  
 186 satellites has 16 channels covering wavelengths of 0.47–13.3  $\mu\text{m}$  and performs full-disk and  
 187 Japan-area observations every 10 and 2.5 min, respectively, from GEO at 140.7° E longitude  
 188 (Bessho et al., 2016). Visible and NIR observations are also performed at high spatial

191 resolutions of 0.5–1.0 km, with SWIR to IR at 2 km, which have advantages in aerosol  
 192 property retrieval and cloud masking.  
 193 Lim et al. (2018) developed the AHI Yonsei aerosol retrieval (YAER) algorithm and  
 194 provided two retrieval results with 6 km × 6 km resolution based on MRM and ESR using  
 195 SWIR data. Aerosol property retrieval using VIS channels requires accurate surface  
 196 reflectance, for which MRM and ESR are useful, with the main difference between the two  
 197 lying in the surface-reflectance estimation method.  
 198 The MRM applies the minimum-reflectance technique over both land and ocean (Lim et al.,  
 199 2018), with surface reflectance being estimated by finding the minimum reflectance in each  
 200 pixel over the past 30 day window, giving the Lambertian equivalent reflectance (LER; Kim  
 201 et al., 2016; Lim et al., 2018). This method takes the bidirectional characteristics of surface  
 202 reflectance into consideration by obtaining surface reflectance at each observation time over  
 203 the 30-day search window. However, the method assumes that there is more than one clear  
 204 day **during the search window** and that surface reflectance does not change; otherwise, it is  
 205 affected by clouds and/or the BAOD (Kim et al., 2014; Kim et al., 2021).  
 206 According to the ESR method, land-surface reflectance in the VIS region is constructed  
 207 from the Top of Atmosphere (TOA) reflectance at 1.6 μm wavelength, based on the NDVI  
 208 for SWIR and the fraction of urbanization and cropland (Levy et al 2013; Gupta et al., 2016;  
 209 Zhong et al., 2016; Lim et al., 2018). Ocean-surface reflectance is estimated from the Cox  
 210 and Munk BRDF model (Cox and Munk, 1954). Chlorophyll-a concentrations are considered  
 211 in addition to Chlorophyll-a concentration data  
 212 (<https://www.eorc.jaxa.jp/ptree/userguide.html>) from Japan Aerospace Exploration Agency  
 213 (JAXA) (Murakami et al., 2016) and interpolated for the 10-min AHI intervals. For  
 214 unretrieved pixels, the less contaminated chlorophyll-a concentration value of 0.02 mg m<sup>-3</sup> is  
 215 used. Details of the methodology can be found in Lim et al. (2018).

216 **2.2 GOCI aerosol algorithm**

217 GOCI is an ocean color imager in GEO launched onboard COMS in 2010 and observes the  
 218 East Asia region at an hourly interval with 500 m × 500 m resolution (Choi et al., 2012). It has  
 219 eight bands in the VIS and NIR regions, which is advantageous for aerosol retrieval. Two  
 220 versions of GOCI Yonsei aerosol algorithms have been developed, referred to as V1 and V2  
 221 (Lee et al., 2010; Choi et al., 2016, 2018). In the case of V1, surface reflectance is estimated  
 222 by the MRM using LER for the past 30 days over land, and the Cox and Munk BRDF model  
 223 over oceans. In V2, ocean-surface reflectance is estimated by the same method, but land-  
 224 surface reflectance is improved by using an accumulated long-term database. To minimize  
 225 the impact of BAOD (the weakness of the MRM), a monthly surface-reflectance database  
 226 was constructed using all of the LERs over the past five years, but it cannot reflect  
 227 unexpected changes in surface conditions. However, a well-established climatological  
 228 database allows aerosol property retrieval in near-real-time with reasonable accuracy.  
 229

230 **3. Data fusion methods**

231 Satellite-derived AODs have different error characteristics depending on NDVI, scattering  
 232 angle, and so on (Choi et al., 2016, 2018; Lim et al., 2018). Over oceans, ESR AODs are  
 233 more accurate than MRM AODs. However, the accuracy of GOCI AODs was dependent on  
 234 the NDVI values, which represent surface condition in terms of vegetation. V1 has a negative  
 235 bias, and V2 has a mostly a positive bias (Choi et al., 2018). In this study, we developed

삭제함: at 550 nm

삭제함: Knapp et al., 2002; Wang et al., 2003; Kim et al., 2008; Choi et al., 2016, 2018; Kim et al., 2016; Lim et al., 2018). This method

삭제함: during the search window

삭제함: background aerosol optical depth (

삭제함: ;

삭제함:

삭제함: is

삭제함: Hsu et al., 2004; Lee et al., 2012; Jackson et al., 2013; Choi et al., 2016, 2018; Lim et al., 2018; Sayer et al., 2018). Chlorophyll-a

[4] 위트 이동함: The MRM gives better accuracy over brighter surfaces such as urban areas, while the ESR method gives better accuracy over areas of dense vegetation (Lim et al., 2018). However, there is a critical surface reflectance at which aerosol signals disappear, depending on the single-scattering albedo (Kim et al., 2016). Over the ocean, both the MRM and ESR methods give high accuracy, but ESR results are robust with the Cox and Munk model. The MRM requires more computational time than the ESR method to estimate surface reflectance, as it requires data for the past 30 days, and LER needs to be calculated using a radiative transfer model. The ESR method estimates surface reflectance from the observed TOA reflectance at 1.6 μm wavelength using empirical equations including the NDVI. The advantage of MRM is that stable surface reflectance values can be obtained regardless of surface type. However, due to the influence of BAOD, surface reflectance tends to be overestimated, with satellite-derived AOD data thus being underestimated (Kim et al., 2014). On the other hand, the ESR method uses TOA reflectance at 1.6 μm wavelength to detect surface signals, which is less sensitive to fine particles and BAOD. However, when aerosols such as yellow dust with coarse particles are transported from the Taklamakan and Gobi deserts, the BAOD effect also applies to the ESR method. The ESR method is also more likely to be affected by snow surfaces than the MRM, as snow reduces reflectivity around the 1.6 μm wavelength (Negi and Kokhanovsky, 2011). The ESR method also has the disadvantage of giving noisy results over bright surfaces such as desert. However, its fast surface-reflectance estimation enables near-real-time retrieval based on the AHI YAER algorithm.

서식 지정함: 영어(미국)

삭제함: ere

삭제함: d

삭제함: , according to

삭제함: .

삭제함: for V1

삭제함: for V2

279 optimal AOD products at 550 nm in East Asia by fusing four individual retrievals, i.e. two  
 280 AHI aerosol products from the MRM and ESR methods, and two GOCI products from V1  
 281 and V2.

### 282 3.1 Spatio-temporal matching

283 The AHI and GOCI have different spatial pixel locations and temporal resolutions, so it is  
 284 necessary to match their spatio-temporal resolutions before data fusion. GOCI and AHI  
 285 AODs have the same spatial resolution of 6 km × 6 km, but the two satellites are located at  
 286 128.2° E and 140.7° E, respectively, at the equator. Spatial pixel matching is therefore  
 287 required. However, satellite-derived AOD represents total-column extinction, so AOD  
 288 retrieved by the two sensors is not significantly affected by satellite position. To merge the  
 289 different satellite spatial pixel coverages, the GOCI pixel was re-gridded to match AHI pixels  
 290 for full-disk observation, with up to 4 GOCI AOD pixels being used with average values  
 291 considered representative of pixel values. If more than half of the AHI AOD pixels did not  
 292 exist out of the maximum 6 AHI data per hour, it is regarded as cloud contaminated pixels  
 293 and an additional cloud removal process is performed. This process applies to both the MRM  
 294 and ESR method, to remove the AHI's additional cloud-contaminated pixels in products of  
 295 both GOCI V1 and V2, which have a disadvantage in cloud masking due to their lack of IR  
 296 channels. When three or more pixels were available for generating AHI data at 1 hour  
 297 intervals, hourly AOD values were estimated as the medians of pixel values.

### 298 3.2 Ensemble-mean method

299 Here, AMR represents AHI MRM AOD, AES represents AHI ESR AOD, GV1 represents  
 300 GOCI V1 AOD, and GV2 represents GOCI V2 AOD. We performed data fusion using AMR,  
 301 AES, GV1, and GV2 data within 1 hour intervals for which additional-cloud masking was  
 302 performed. The ensemble-mean is the mean of the ensemble member over a specific time.  
 303 The ensemble members are AMR, AES, GV1, and GV2 based on two satellite instruments  
 304 and two different surface-estimation methodologies. Table 1 provides the satellite-derived  
 305 AOD used for ensemble-mean and MLE fusion.

306 Fusion was performed only when a pixel of an ensemble member was used for all fusions.  
 307 Fusion 1 (F1) included the two AHI products of AMR and AES, and two GOCI products of  
 308 GV1 and GV2. Fusion 2 (F2) involved the calculation of the YAER algorithm by the fusion  
 309 of AES and GV2, both of which have the advantage of producing data in near-real-time.  
 310 Fusion 3 (F3) merged AMR and AES to estimate AOD over a wide area, and Fusion 4 (F4)  
 311 involved a comparison with F1 to determine how accuracy varied with decreasing number of  
 312 ensemble members, as summarized in Table 1.

### 313 3.3 MLE method

314 Similarly, FM1, FM2, and FM3 is the result of MLE fusion corresponding to F1, F2, and F3  
 315 as in ensemble mean, respectively (see Table 1).

316 The MLE method provides a means of weighting and averaging based on errors evaluated  
 317 with AERONET ground-based measurements (Nirala, 2008; Xu et al., 2015; Xie et al., 2018).

318 This method employs the following equations:

$$\tau_i^{MLE} = \frac{\sum_{k=1}^N R_{i,k}^{-2} \tau_{i,k}}{\sum_{k=1}^N R_{i,k}^{-2}} \quad (1)$$

삭제함:

삭제함:

서식 지정함: 영어(미국)

삭제함: Also, Table 1 shows the

삭제함: is

삭제함: involving all satellite-derived AOD, and FM2 involves AER and GV2 for near-real-time operation. FM3 includes AMR and AES, enabling wide-area (70°-150 °E, 0°-50°N) observation...

삭제함:

$$R_{i,k} = \sqrt{\frac{\sum_{i=1}^M (s_{i,k} - g_i)^2}{M}} \quad (2)$$

327 where  $\tau_i^{MLE}$  represents the fused AOD;  $\tau_{i,k}$  represents the mean AOD at grid point  $i$  from the  
 328 satellite-derived AOD product  $k$ , where  $k$  is the index for different satellite-derived AOD  
 329 products for fusion;  $R_{i,k}$  represents the root-mean-square error (RMSE) at grid point  $i$  for the  
 330 satellite-derived AOD product  $k$ ;  $N$  is the number of all AOD data;  $g_i$  represents the mean of  
 331 ground-based AOD at grid point  $i$  from the AERONET (collocated temporal mean);  $s_{i,k}$   
 332 represents the mean of satellite derived AOD products ( $k$ ) at grid points of the AERONET  
 333 (collocated spatial mean); and  $M$  is the number of pairs of  $s_{i,k}$  and  $g_i$ .

334 For RMSE estimation, bias correction, validation, and error estimation (details in Sec.5),  
 335 AERONET Version 3 Level 2.0 aerosol products were used for ground truth (Giles et al.,  
 336 2019; Smirnov et al., 2000; Holben et al., 2001). RMSE and bias correction value for each  
 337 satellite product (details in Sec.3.4) required for MLE fusion were calculated through  
 338 comparison with AERONET from Apr. 2018 to Mar. 2019 excluding EMeRGe period. The  
 339 number of AERONET sites used for validation and error estimation in this study, was 35  
 340 during the KORUS-AQ campaign, and 22 during the EMeRGe campaign, for AHI and GOCI  
 341 products.

342 Satellite observation can cover wide areas, but the ground observation instrument cannot  
 343 cover all satellite observed areas. Therefore, a RMSE model was constructed for AOD, time,  
 344 and NDVI through comparative validation with AERONET observation as shown in Figure 1.  
 345 For MLE over wide areas without ground measurements, the calculated RMSE from AOD,  
 346 time, and NDVI bins was applied for every satellite pixel. We excluded points that AOD  
 347 differences with respect to AERONET data (dAOD) were  $> 2$  standard deviations (SD) to  
 348 remove outliers and to consider only the more stable RMSE values. According to Figure 1, if  
 349 the AOD is less than 0.5, RMSE is about 0.1 with respect to all NDVI bins, but if the AOD is  
 350 greater than 0.5, the overall RMSE value becomes large. All products excluding AES show  
 351 large variations for high NDVI and high AOD bin as shown as the red square in Figure 1,  
 352 especially for 02 UTC and 05 UTC of two GOCI products and 00 UTC in AMR product.  
 353 This is because the two GOCI products and AMR are relatively less accurate for densely  
 354 vegetated areas, along with sampling issues.

### 355 3.4 Bias correction

356 AOD follows a log-normal distribution (Sayer and Knobelspiesse, 2019), but dAOD for  
 357 each satellite product follow a Gaussian distribution. The quantile-quantile (Q-Q) plot is a  
 358 graphical statistical technique that compares two probability distributions with each other.  
 359 The x-axis represents the quantile value of the directly calculated sample, and the y-axis  
 360 represents the Z-score. Here, the Z-score is a dimensionless value that makes a statistically  
 361 Gaussian distribution and shows where each sample is located on the standard deviation. That  
 362 is, when Z-score of 1 and 2 represent 1 SD and 2 SD, respectively. In addition, as the Q-Q  
 363 plot shows a linear shape, the sample follows a Gaussian distribution.

364 Figure 2 shows dAOD divided by SD analyzed for each satellite product, for the period  
 365 from April 2018 to March 2019, excluding the EMeRGe campaign, which shows a similar  
 366 pattern to the standard Gaussian distribution. However, if the theoretical quantile values are  
 367 greater than 0.5, then the sample quantile values are smaller than the standard Gaussian  
 368 values. Also, when the theoretical quantile is less than 0.5, the opposite results are shown.

삭제함: B  
 서식 있음: 들여쓰기: 첫 줄: 0.5 글자, 탭: 18.8 글자(없음)  
 삭제함:  
 삭제함: AERONET offers freely available spectral AOD measurements every 15 min (or less) at numerous monitoring sites worldwide, with an uncertainty of 1%–2% under cloudless conditions (Smirnov et al., 2000; Holben et al., 2001). Newly updated  
 삭제함: Newly updated AERONET Version 3 Level 2.0 AOPs with additional cloud screening and quality control were selected for validation purposes (Giles et al., 2019). Each satellite product ...  
 삭제함: ↵

삭제함: ower  
 삭제함: show  
 삭제함: to be  
 삭제함: is  
 삭제함: on  
 삭제함: in  
 삭제함: in  
 삭제함: s  
 삭제함: ↵  
 삭제함: (Sayer et al., 2013)

삭제함: is  
 삭제함: analysis  
 삭제함: . Also, Figure 2

392 Thus, the sample quantiles are more skewed at both sides than the theoretical quantile, but the  
393 respective satellite product follows the Gaussian distribution.

394  
395 The bias center for each satellite product was calculated differently for time and NDVI bins  
396 through Gaussian fitting in Figure 3 of the dAOD divided by SD (except for 2SD and higher),  
397 and subtracted from respective product for correction. Data beyond 2 SD of dAOD were  
398 excluded to prevent a change in bias trends due to AOD errors caused by cloud shadows and  
399 cloud contamination. This process was performed before applying the MLE method, which  
400 allows compensation for systematic bias that is difficult to obtain directly in MLE.

### 402 3.5 Evaluation of aerosol products during two field campaigns

403 The performance of the respective satellite product and fused products was analyzed in two  
404 field campaigns: the KORUS-AQ of 1 May 2016 to 12 Jun 2016 ([https://www-  
405 air.larc.nasa.gov/missions/korus-aq/](https://www-air.larc.nasa.gov/missions/korus-aq/)), and the EMeRGe of 12 Mar 2018 to 8 Apr 2018  
406 (<https://www.halo.dlr.de/science/missions/emerge/emerge.html>). KORUS-AQ was an  
407 international multi-organization mission to observe air quality across the Korean Peninsula  
408 and surrounding waters, led by the US National Aeronautics and Space Administration  
409 (NASA) and the Korean National Institute of Environmental Research (NIER) (Crawford et  
410 al., 2021). EMeRGe aimed to investigate experimentally the patterns of atmospheric transport  
411 and transformation of pollution plumes originating from Eurasia, tropical and subtropical  
412 Asian megacities, and other major population centers. GEO satellite data played an important  
413 role in these campaigns; e.g., data assimilation for chemical transport models and tracking  
414 aerosol plumes (Saide et al., 2014, 2010; Pang et al., 2018).

415 In this study, we used satellite-derived GOCI and AHI AODs, with a spatial resolution of 6  
416 km × 6 km, and temporal resolutions of 1 hour and 10 minutes, respectively. Spatio-temporal  
417 correlation between satellite-derived AOD and AERONET AOD involved data averaged over  
418 all satellite pixels within a 25 km radius of the AERONET site, and AERONET AOD  
419 averaged over ±30 minutes from the satellite observation time. As validation metrics,  
420 Pearson's correlation coefficient, median bias error (MBE), the fraction (%) within the  
421 expected error of MODIS DT (EE), and Global Climate Observing System requirement for  
422 AOD (GCOS: GCOS, 2011) were applied. The accuracy requirement of GCOS for satellite-  
423 derived AOD at 550nm is 10% or 0.03, whichever is larger. The EE provided by the MODIS  
424 DT algorithm (EE as  $\pm 0.05 \pm 0.15 \times \text{AOD}$ ; (Levy et al., 2010)) was used for consistent  
425 comparison with previous studies.

426 Table 2 shows the validation metrics of the respective product during the two field  
427 campaigns. The collocation points for validation with AERONET of two AHI and two GOCI  
428 products were not significantly different. %EE and %GCOS of AES and AMR showed better  
429 accuracy than GV1 and GV2 during the KORUS and the EMeRGe periods. In terms of MBE,  
430 GV2 is 0.008 and -0.001, which shows during the KORUS-AQ and the EMeRGe periods  
431 close to zero. Additionally, further analyzes of the respective satellite product are carried out  
432 along with fused products in Section 5.

## 434 4. Results

435 Figure 4 (a) shows the average AOD of FM1 (MLE method with all products) during the  
436 KORUS-AQ period, and Figure 4 (b-e) shows the respective difference of the average AOD

삭제함: In the Q-Q plot, the overall linear relationship is well represented within 1 SD. There is no linear relationship between 1 SD (black solid line) and 2 SD (black dotted line), but soon again appears in a linear relationship.

삭제함: (

삭제함: )

서식 지정함: 강조 없음

삭제함: To minimize the effect of outliers in this process, data beyond 2 SD were excluded and applied differently according to NDVI and time. Data beyond 2 SD of dAOD were excluded to

삭제함: pixels contaminated by

삭제함: s

삭제함: Bias correction values are provided in Figure 3 where Gaussian center is calculated differently for NDVI, time, and respective satellite products, through the Gaussian fitting of the dAODs. Through this process of shifting the obtained Gaussian center values to match the 0 in bias, the systematic bias of the algorithms was corrected. ...

삭제함: ↵

서식 지정함: 글꼴: 12 pt

삭제함: Here

삭제함: applied

삭제함: ↵

In this study, s

삭제함: easy

삭제함: , respectively

삭제함: k

삭제함: in

of AMR, AES, GV1, and GV2, with respect to FM1. FM1 was selected as the representative fused product as FM1 used all four satellite-derived products for fusion with bias correction. The result of the comparison with the respective satellite product (Figure 4 (b-e)) shows different features. AMR shows a negative bias over the ocean but shows similar results to FM1 over land, while AES shows a different tendency in northern and southern China. GV1 tends to show opposite pattern to AES, and GV2 shows positive bias over the ocean and results in similar pattern to FM1 over the land. In the west of the Korean peninsula, AES AOD has a positive offset compared to FM1. Although the AES algorithm considers the fraction of urbanization, there is still a tendency to have a positive AOD offsets. The main reason why AES results show different patterns is the different estimation process of the land surface reflectance from that of other products.

On the other hand, in GV1, the AOD over the Manchurian region has a positive offset compared to FM1. This is because the aerosol signal is small over bright surface, making it difficult to retrieve aerosol properties. These features tend to be alleviated in GV2, where the surface reflectance and cloud removal process were improved.

Figure 5 shows the same result as Figure 4 except for the EMerGe period. The AMR and AES AODs appeared high in northern China, which is thought to be the snow contaminated pixel. The EMerGe period was in March-April, when northern China is more covered by snow compared to the KORUS-AQ period in May-June. On the other hand, for GV1 and GV2, the effect of overestimation with snow contaminated pixel is relatively small, as their snow masking is well performed. However, for the KORUS-AQ period, it seems that the GV1's overestimation of AOD in northern China still remains. Since this analysis (Figure 4 and 5) is for the fusion between the three MRM results and one ESR result, the average field difference is naturally the largest in AES which uses ESR method.

For the characteristics of the average AOD for the two campaign period, high AODs during the KORUS-AQ period were found in eastern China, and Hokkaido as wildfires from Russia were transported to Hokkaido (Lee et al., 2019). Meanwhile, during the EMerGe period, high AOD is shown over the Yellow sea as aerosols were transported from China to the Korean peninsula through the west coast, contrary to the KORUS-AQ period. Overall, the average AODs for the EMerGe are less smooth than those of the KORUS-AQ period. This is because the EMerGe period was shorter than that of the KORUS-AQ, and the retrieval accuracy was lower due to the bright surface.

## 5. Validation, comparison, and error estimation against AERONET

### 5.1 Validation for fused AOD products with AERONET

The spatio-temporal matching method between fused AOD and AERONET was performed as mentioned above in Section 3.5, and the statistics indices used for verification are also the same. Validation indices of fused products with AERONET AOD during the two campaign periods are summarized in Table 3. During the KORUS-AQ, fused AODs have better accuracy of than respective satellite product in terms of %EE and %GCOS. The %EE and %GCOS of AES, which showed the best accuracy among the respective product, are 63.5% and 43.6%, which are poor than the worst accuracy of the fused AOD. All RMSE has been improved except for FM2. The RMSE of FM2 is higher than RMSE of respective satellite product by 0.001. Although all MBEs show different patterns, the deviation of the fused products tends to be smaller. GV2 and F2 show MBE of 0.008, close to zero.

- 삭제함: , F1, F2, F3, F4, FM2, and FM3
- 삭제함: The reason for selecting
- 삭제함: site i
- 삭제함: that
- 삭제함: were used,
- 삭제함: and
- 삭제함: was also performed
- 삭제함: It is also best to evaluate respective satellite product relatively since all satellite-derived products have been used. ...
- 삭제함: is overestimated
- 삭제함: overestimate AODs
- 삭제함: is
- 삭제함: overestimated
- 삭제함: Also, the difference was the least for the F1 result that differs only in the fusion method under the same configuration as FM1, and the F4 result (AMR, AES, and GV2) showed similar results. F3 and FM3, fusion products using AHI only, retain relatively strong AES features, thus their differences from FM1 (Figure 4 (h) and (k)) showing similar pattern as AES cases in Figure 4 (c)....
- 삭제함: overestimated
- 삭제함: AODs
- 삭제함: .
- 삭제함: FM1, the MLE product of F1, showed the most similar results naturally, followed by F4...
- 삭제함: However,
- 삭제함: s
- 삭제함: a
- 삭제함: The Gangneung-Wonju National University site (Gangneung-WNU; 128.87°E, 37.77°N) lies on the eastern side of the Korean Peninsula and it is one of the regions with low aerosol loadings. The AOD frequency distribution generally follows a log-normal distribution, and it is important to estimate low AOD levels exactly to increase its accuracy. Therefore, we evaluated whether the fused products ... [1]
- 삭제함: Error estimation
- 삭제함: validation
- 삭제함: For validation and error estimation, AERONET aeros ... [2]
- 삭제함: Spatio-temporal correlation between satellite-derived ... [3]
- 삭제함: ex
- 삭제함: of fused products
- 삭제함: The MODIS DT algorithm provided EE as  $\pm 0.05 \pm 0$  ... [4]
- 삭제함: In
- 삭제함: korus
- 삭제함: %EE and %GCOS
- 삭제함: fused AODs
- 삭제함: s
- 삭제함: of
- 삭제함: , and even
- 삭제함: .
- 삭제함: which has the lowest accuracy among fused products,
- 삭제함: 0.001

618 Next, %EE for the EMerGe period exceeded 60.0, with AMR having the best accuracy of  
 619 69.4. Likewise, %GCOS was also the highest with 52.4, which showed better accuracy than  
 620 the fused product. In terms of MBE, GV2 was the best, with -0.001. The fused products did  
 621 not have the best statistical values, but they show overall better statistical values.  
 622 Figure 6 shows the %GCOS for the respective satellite product and fused products at each  
 623 validation site during each campaign. In Figure 6(a), for the KORUS period, F1 and FM1  
 624 show the highest % GCOS at 20 sites out of 35. Other than the fused result, AES shows the  
 625 highest %GCOS at 13 sites, which are mostly dense vegetation-area and coastal sites. On the  
 626 other hand, during EMerGe period, the %GCOS of fused products was highest at 7 sites out  
 627 of 22, while respective satellite product showed at the rest of the sites in similar proportions.  
 628

629 **5.2 Error estimation**

630 Differences between satellite products and AERONET, dAOD values were analyzed in  
 631 terms of NDVI and observation times (Figure 7). Figure 7 (a) and (d) shows the respective  
 632 satellite product, Figure 7 (b) and (e) the ensemble-mean product, and Figure 7 (c) and (f) the  
 633 MLE fusion results, with each filled circle representing the mean of 500 and 400 collocated  
 634 data points sorted in terms of NDVI for the KORUS-AQ and the EMerGe campaigns,  
 635 respectively. Figure 7 (a) shows different biases for each satellite product, with AMR and  
 636 GV1 being negative, AES and GV2 being positive. The errors are close to zero for both the  
 637 ensemble-mean and MLE products except for FM2 as a result of the fusion process.  
 638 When the NDVI is small, the Gaussian center for GV2 dAOD was close to zero, but when the  
 639 NDVI is large, the Gaussian center was negative as shown in Figure 3. The bias correction  
 640 effect of GV2 shows a small effect for small NDVI bins and a large effect for large NDVI  
 641 bins. In fact, the collocated dAODs of FM2 show close to zero when the NDVI bins are  
 642 greater than 0.4 (in Figure 7 (a)).

643 During the EMerGe campaign (right column, Figure 7), the two AHI and two GOCI  
 644 products show negative biases, and even the ensemble-mean results have negative biases. The  
 645 ensemble-mean does not include any bias correction, meaning that the error characteristics of  
 646 each original satellite product are intact. The MLE products display improved biases in terms  
 647 of NDVI, which are close to zero because the bias was corrected for in the MLE process.  
 648 During the EMerGe period, the collocated dAOD values at NDVI around 0.1 have a  
 649 negative value for all satellite-derived products (especially AHI products), and GV1 has a  
 650 negative value for bins where NDVI is greater than 0.2. During the EMerGe period, the  
 651 collocated dAOD values at NDVI around 0.1 show negative values for all respective product  
 652 (especially AHI products), and dAOD for GV1 shows negative values for NDVI bins greater  
 653 than 0.2. The fused products tend to have error close to zero except for F3 and FM3. In terms  
 654 of F3, the collocated dAOD value around 0.1 of the NDVI bin has negative values for both  
 655 AMR and AES, so the collocated dAOD of F3 remain negative. Gaussian center values for  
 656 FM3, AMR and AES (in Figure 3) are close to zero for NDVI at around 0.1, so the bias  
 657 correction effect is small. This can be explained by the fact that the collocated dAOD for  
 658 NDVI at around 0.2 during the EMerGe period is closer to zero in FM3 than in F3.

659 The median bias of the AOD products over the observation time was analyzed as shown in  
 660 Figure 8 where the left column represents the KORUS-AQ and the right column the EMerGe  
 661 campaign, with filled circles representing median values, and the error bar being  $\pm 1$  SD. As  
 662 in the KORUS-AQ campaign, the AMR shows a generally negative bias, as in the all-time  
 663 results, and a negative bias also exists in each time zone. In the AES, GV1, and GV2 case,  
 664 positive and negative biases appear differently according to time zones. The  $\pm 1$  SD of the

삭제함: in ...or the EMerGe period exceeded 60.0, with AMR ... [5]

삭제함: EE of [6]

삭제함: byat each validation site for % GCOS ...uringof...ead [6]

삭제함: Results of the comparison with AERONET during the KORUS-AQ are shown in Figure 7, the EE values of AER, AES, G1, and GV2 were 53.2%, 58.0%, 52.2%, and 50.3%, respectively. Fused products have EE values of up to 73.3%, much higher than the respective satellite product. In terms of RMSE, all of the fusion products without F3 and FM3 (validation over a broader area) have a value of 0.128, lower than the minimum value of various satellite products (0.153). Figure 7 (g) and (k) shows relatively scattered patterns compared with other fusion products because they show data fused with only AHI products. EE values for all AERONET products used for validation are shown in Figure 8, where AHI covers a broader area than GOCI. The accuracy is low over northern India and the Indochina Peninsula. However, EE values after fusion (Figure 8 (g, k)) are higher than those of the respective satellite product. The fused results (Figure 8 (g, k)) of two AHI products display high EE values within the domains of GOCI and other fusion products. The scattered fusion results based on two AHI products (Figure 7) can thus be attributed to issues at these particular sites, rather than to the satellite products themselves. Results of the comparative validation with AERONET during the EMerGe campaign (Figure 9) indicate that, overall, fusion products improve the statistical metrics, as in the KORUS-AQ case. The validation result for each satellite product shows that the maximum value of EE is 63.4%–68.0% after fusion. Thus, the EE increases as other statistics improve, including an RMSE decrease from 0.162 to 0.149. However, despite the MLE fusion (FM1-3) with bias correction using the Gaussian center values, MBE shows a rather poor result. This is because the Gaussian center value used for error correction does not work properly during the EMerGe campaign. Low NDVI in summer is generally seen for bright surfaces such as deserts, but low NDVIs are present in many areas, other than deserts during the EMerGe campaign period. To improve this, it is desirable to use seasonal Gaussian center values.<sup>47</sup> As in the KORUS-AQ campaign, the validation results for the two AHI products and the fusion products based on AHI AODs only are inferior to the results for the fusion products based on GOCI AODs. This is because the validation was performed over wider areas, and problems were noted at specific sites. The fused results showed improved accuracy not only in terms of EE but also in statistical metrics such as RSME, MBE, and MAE. Results for the EMerGe campaign are shown in Figure 10. During that campaign, validation results over brighter surfaces in northern India and the Indochina Peninsula show reduced accuracy, but fusion results show consistently higher EE values than individual satellite products.<sup>47</sup>

삭제함: on the basisin terms of NDVI values [7]

삭제함: 117). Figure 11... (a) and (d) shows the respective sat [8]

삭제함: 8 [9]

삭제함: c) the ensemble-mean product, and Figure 11... (c) af [9]

삭제함: [10]

삭제함: [10]

삭제함: and GV2 converging to almost zero... The errors are [10]

삭제함: FM2 is a fused product using AES and GV2. [10]

서식 있음: 들여쓰기: 첫 줄: 0 글자 [10]

삭제함: GV2 has athe Gaussian center value...or GV2 dAOD [11]

삭제함: 117), the two AHI and two GOCI products show neg [12]

서식 있음: 들여쓰기: 첫 줄: 0 글자 [12]

삭제함: In the EMerGe period, the collocated dD...OD valu [13]

삭제함: 12 ... where the left column represents the KORUS [14]

삭제함: length [14]

847 respective satellite product is larger at local noon and smaller at 00 and 07 UTC when SZA is  
 848 large. Fused products as shown in Figures 8 (b) and (c), have a smaller  $\pm 1$  SD, and the  
 849 collocated  $\Delta$ AOD over the observation time is also close to zero. Meanwhile, FM2 shows the  
 850 same tendency of overestimation for the same reason as in the previous Figure 7(a).  
 851 For the EMERGE period, the collocated  $\Delta$ AOD values of the respective product appear  
 852 closer to zero than KORUS-AQ. Similarly, the collocated  $\Delta$ AOD of the fused products also  
 853 show values close to zero.

854 The error analysis indicates that the results after fusion are more accurate than the results  
 855 obtained using individual satellite product, and fused products accuracy was slightly better  
 856 during KORUS-AQ than EMERGE because more data points were considered. Also, the  
 857 surface was relatively dark during the KORUS-AQ period, thus reduced errors for aerosol  
 858 retrieval than during the EMERGE period.  
 859

### 860 5.3 Time-series analysis of daily mean and hourly AODs

861 The Gangneung-Wonju National University site (Gangneung-WNU; 128.87°E, 37.77°N)  
 862 lies on the eastern side of the Korean Peninsula and it is one of the regions with low aerosol  
 863 loadings. The AOD frequency distribution generally follows a log-normal distribution, and it  
 864 is important to evaluate accuracy for low AOD values. Therefore, we evaluated whether the  
 865 fused products were improved at low AODs. A daily mean time-series and diurnal variation  
 866 comparison of different satellite AOD products against AERONET (on a logarithmic scale)  
 867 are shown in Figure 9 for the Gangneung-WNU site without high AOD events, where most  
 868 point AERONET AODs at 550 nm were  $< 1$  during the KORUS-AQ campaign. Daily mean  
 869 time-series data from the AERONET, ensemble-mean, and MLE products are shown in  
 870 Figure 9 (a-c), where black filled circles and black error bar represent AERONET AOD and  
 871  $\pm 1$  SD of one-day average AERONET AOD. Satellite-derived AODs represented in different  
 872 colors show similar variabilities.

873 Respective satellite product generally shows similar daily-mean AOD distribution to  
 874 AERONET AOD. AMR, GV1, GV2 using MRM technique show similar patterns, and AES  
 875 using SWIR for surface reflectance estimation shows different patterns. The daily-mean AOD  
 876 of AES is more close to AERONET. On the other hand, Figure 9 (b) and (c) representing  
 877 fused AOD show similar patterns overall, but the daily-mean AODs on 11 May show  
 878 different patterns. Here, ensemble-mean products (F1-4) are less accurate than an individual  
 879 AES product, while MLE products (FM1-3) exhibit similar diurnal variation to daily-mean  
 880 AERONET AOD. To further analyze this, the daily-mean AOD is shown in Figure 9 (d-f)  
 881 instead of the hourly AOD for 11-14 May.

882 As in the previous daily-mean AOD results, Figure 9 (d) shows the hourly AES AOD  
 883 variations are close to hourly AERONET, while AMR, GV1, and GV2 tend to underestimate.  
 884 Similarly, as shown in Figure 9 (e), hourly AOD variation of the ensemble-mean products  
 885 shows overall underestimation for 11 May. All ensemble-mean products use AES as an  
 886 ensemble member, but do not sufficiently compensate for the negative biases held by AMR,  
 887 GV1, and GV2. Meanwhile, MLE fused products show similar patterns to the hourly AOD  
 888 variation of AERONET, such as AES outputs. This can be explained in two ways: the effect  
 889 of considering the weighted function based on pixel-level uncertainty (RMSE in this study)  
 890 and the bias correction effects. Figure 1 showed similar RMSE values for all observation  
 891 times when  $\text{AOD} < 0.5$ . Gangneung-WNU site is one of the densely vegetated areas, but if  
 892 the AOD is less or equal to 0.5, there is little sensitivity of RMSE according to NDVI bins.  
 893 That is, regardless of the NDVI, each satellite-specific weighting function used for the MLE

847 **삭제함:** longelargr...r at local noon and shorte...mallr...r at [... [15]

848 **삭제함:** 9

849 **삭제함:** horter length of smaller  $\pm 1$  SD, and the collocated  $\Delta$ D [... [16]

850 **삭제함:** In the EMERGE period, the collocated  $\Delta$ D...OD val [... [17]

851 **삭제함:** In the EMERGE period, the two AHI results have large error  
 852 ranges. GEO satellites perform observations over a specific area with  
 853 a fixed viewing zenith-angle and retrieve AOPs by solar reflectance,  
 854 which means that a specific site has different local time depending on  
 855 its longitude for a given satellite image. Furthermore, there are fewer  
 856 data for the EMERGE period than the KORUS-AQ period, and data for  
 857 northern India and the Indochina Peninsula, which have low  
 858 accuracy, are included in the data for 0100–0300 UTC, indicating  
 859 large errors. In the KORUS-AQ period, the data fraction for a  
 860 specific site is not as large as in the EMERGE period, so this problem  
 861 does not arise. ... Taylor diagrams for accuracy evaluation of AOD  
 862 Taylor diagrams for accuracy evaluation of AOD data fusion  
 863 products are shown in Figure 13. The Taylor diagram is a graphic  
 864 summary of how closely satellite retrievals match observations. Here,  
 865 match-up values were respective and fusion AOD products, and the  
 866 matching up data were AERONET AOD. Correlation coefficient, SD,  
 867 RSME, and EE values were used as the matching criteria. The  
 868 correlation coefficient is shown in green (Figure 13) with a polar  
 869 angle, the SD is shown in the radial distance on the black x- and y-  
 870 axes, and RMSE is the proportional cyan circle from the "AERONET"  
 871 point on the x-axis. The EE value, which can evaluate the stability of  
 872 AODs, is shown for each color. AMR, AES, GV1, GV2, F1, F2, F3,  
 873 F4, FM1, FM2, and FM3 are indicated by different symbol,  
 874 respectively. <sup>42</sup>

875 Correlation coefficients are all around 0.8–0.9 with no significant  
 876 differences for respective and fusion AODs. However, results after  
 877 fusion show slightly better than respective satellite product accuracy  
 878 in terms of SD, RMSE, and EE values. <sup>42</sup>

879 Standard deviation values indicate that products that lie outside the  
 880 purple dotted half-circle are larger than the SD of AERONET. In the  
 881 AHI case, the SD appears smaller than GOCl values because it tends to  
 882 underestimate values at high AOD. Similarly, RMSE values are  
 883 lower after fusion. <sup>42</sup>

884 The EMERGE period was from March to April, when the surface is  
 885 brighter in East Asia than during the KORUS-AQ period of May to  
 886 June. The accuracy during the EMERGE period is therefore similar to  
 887 or slightly poorer than that of the KORUS-AQ period. The  
 888 correlation coefficient shows similar values, but the SD, RMSE, and  
 889 EE values are slightly lower. Again, the accuracy of the validation  
 890 metrics is improved by fusion. <sup>42</sup>

891 **삭제함:** Taylor diagrams for accuracy evaluation of AOD data  
 892 products are shown in Figure 13. The Taylor diagram is a graphic  
 893 summary of how closely satellite retrievals match observations. Here,  
 894 match-up values were respective and fusion AOD products, and the  
 895 matching up data were AERONET AOD. Correlation coefficient, SD,  
 896 RSME, and EE values were used as the matching criteria. The  
 897 correlation coefficient is shown in green (Figure 13) with a polar  
 898 angle, the SD is shown in the radial distance on the black x- and y-  
 899 axes, and RMSE is the proportional cyan circle from the "AERONET"  
 900 point on the x-axis. The EE value, which can evaluate the stability of  
 901 AODs, is shown for each color. AMR, AES, GV1, GV2, F1, F2, F3,  
 902 F4, FM1, FM2, and FM3 are indicated by different symbol,  
 903 respectively. <sup>42</sup>

904 Correlation coefficients are all around 0.8–0.9 with no significant  
 905 differences for respective and fusion AODs. However, results after  
 906 fusion show slightly better than respective satellite product accuracy  
 907 in terms of SD, RMSE, and EE values. <sup>42</sup>

908 Standard deviation values indicate that products that lie outside the  
 909 purple dotted half-circle are larger than the SD of AERONET [... [18]

910 **서식 있음:** 양쪽

911 **삭제함:** estimatevaluate accuracy for low AOD levels...alu [... [19]

912 **삭제함:** reflectancetechnique show similar patterns, and AES [... [20]

913 **서식 있음:** 들여쓰기: 첫 줄: 0 글자

914 **삭제함:** that similarly to the previous daily-mean AOD resul [... [21]

fusion has a similar value for all satellite-derived products. The difference between the ensemble-mean and the MLE fused products is due to the bias correction considered in the MLE fusion. For example, the FM3 states that AMR has a large negative bias in the afternoon and AES has a negative bias in the morning. With the bias correction of AES and AMR respectively in the morning and afternoon, FM3 is calibrated in a direction to compensate the underestimated AOD. The effect of bias correction and MLE fusion agreement varies depending on the NDVI and AOD loading for each pixel. If bias correction was not performed in the case on 11 May, the MLE fusion output shows very similar values to F3.

The MLE products were implemented in a way to improve accuracy for the low AOD region more critically than in the high AOD region by systematic bias correction. In general surface reflectance estimated by the MRM is affected by BAOD, to result in a negative bias in AOD. On the other hand, the AES uses TOA reflectance at 1.6 μm wavelength to estimate surface reflectance and is therefore less affected by BAOD, and shows higher AOD than AMR and the two GOCI AODs. Furthermore, AOD retrieval over vegetated areas is more accurate with the ESR method. This result is consistent with previous studies of aerosol retrieval in the VIS region (Levy et al., 2013; Gupta et al., 2019; Hsu et al., 2019).

#### 5.4 Accuracy evaluation for AHI products of the outside of GOCI domain

In this section, the AMR, AES, F3, and FM3 products were evaluated at 34 sites within the 0-50°N and 70-150°E except for the GOCI domain as shown in Figures 4 and 5 (112-148°E, 24-50°N). The evaluation results are summarized in Table 4 in terms of N, R, RMSE, MBE, and GCOS fraction. The RMSE and Gaussian center values within the GOCI domain were used in the MLE fusion in this section (see Figures 1 and 3). Table 4 shows the %GCOS and RMSE values with poor accuracy than the validation results for the GOCI coverage as listed in Table 4. In addition, BME during the KORUS-AQ and the EMerGe period was -0.098 and -0.135 for AMR, and 0.130 and -0.055 for AES, respectively, which show very poor accuracy. This can be explained by the cloud contamination issue at sites near the equator, including Thailand. In addition, since AMR cannot collect enough clear pixels for the estimation of LER, which can cause errors. Furthermore, MRM does not work well over desert areas. On the other hand, AES has issues with poor accuracy over bright pixels such as desert and snow contaminated areas. Second, there are many areas where the coastline is complex as in Hong Kong, and the surface elevation is uneven as in Himalayas. However, there is a bias of -0.055 during the EMerGe period for AES, but the %GCOS was the highest with 34.1, which is considered significant. F3 and FM3 show similar patterns for the KORUS-AQ and the EMerGe period. The accuracy of F3 is better than that of FM3 because the previously mentioned issue for the bias correction has worked incorrectly, as the RMSE and bias correction values used were from the data in the untrained area.

#### 6. Summary and conclusion

Various aerosol algorithms have been developed for two different GEO satellites, AHI and GOCI. Retrieved AOD data have advantages and disadvantages, depending on the concept of the algorithm and surface-reflectance estimations. In this study, four aerosol products (GV1, GV2, AMR, and AES) were used to construct ensemble-mean and MLE products. For the ensemble-mean, this study presented fusion products taking advantage of overlap region,

삭제함: In other words, it can be said that (The difference between ... [22])

서식 있음: 들어쓰기: 첫 줄: 0.5 글자

삭제함: andto result in AOD thus shows ... [23]

서식 지정함: 영어(영국)

삭제함: 3

서식 있음: 표준, 들어쓰기: 첫 줄: 0.5 글자

삭제함: on

서식 지정함: 강조 없음

삭제함: a total of

서식 지정함: 강조 없음

삭제함: (

서식 지정함: 강조 없음

삭제함: ;

서식 지정함 ... [24]

삭제함: were calculated within the GOCI domain ...see Fig ... [25]

서식 있음: 표준

서식 지정함: 글꼴: (영어) Times New Roman

삭제함: In this section, the accuracy of AHI products in the GOCI domain was evaluated. Table 2 shows all sites and co-located sites with GOCI for AMR, AES, F3, and FM3, where values exist for a wide area, and summarizes them for the KORUS-AQ and the EMerGe periods. First, during the KORUS-AQ period, it can be seen that the number of collocated data has decreased by about 2000 points. By reducing the validation area, R, RMSE, MBE, and %EE were improved. RMSE is 0.150 and 0.145, which is better than 0.153 and 0.176 of GV1 and GV2, and there is a difference of more than 10% in %EE. Likewise, the results of fusion products are also improved. However, there is a slightly different trend for the EMerGe period. First of all, by reducing the area, the percentage of reduced points is more than 60%, which is more than the 30% for the KORUS-AQ period. In existing AMR and AES products, the statistical value tends to increase as the area becomes smaller. However, the fusion product's accuracy is rather decreased for the GOCI coverage. For AMR and AES, MBE and RMSE are similar to or better than GV1 and GV2, and %EE are higher than GV1 and GV2. However, in contrast to the KORUS-AQ period, the bias characteristics of AMR and AES are also negative, so the accuracy of F3 is inferior to the existing products. Meanwhile, the decrease in the accuracy of the FM3 product can be explained by difficulty to obtain accurate statistics due to higher weight in other areas beyond GOCI domain.

삭제함: based ofom...two different GEO satellites, AHI,...a ... [26]

삭제함:

1256 accuracy, and near-real-time processing. For MLE products, bias corrections for different  
 1257 observation times and surface type were performed considering pixel-level errors, and the  
 1258 synergy of fusion between GEO satellites was successfully demonstrated.  
 1259 Validation with the AERONET confirmed that averaging ensemble members improved  
 1260 most of statistical metrics for ensemble products, and consideration of pixel-level uncertainty  
 1261 further improved the accuracy of MLE products. For optimized AOD products in East Asia,  
 1262 NDVI and time-dependent errors have been reduced. The ensemble-mean and MLE fusion  
 1263 results show consistent results with better accuracy.  
 1264 By comparing F1 and F4, we can see the accuracy changes depending on the number of  
 1265 members used in the ensemble-mean. During the KORUS-AQ period, poor accuracy of each  
 1266 member for ensemble averaging made difficult to find true features. The accuracy of F4 was  
 1267 higher than that of F1, which shows the effect of GV1's large bias during the KORUS-AQ  
 1268 period. On the other hand, for the EMERGe period, the difference between F1 and F4 appears  
 1269 small because the respective ensemble member's accuracy was better. Both near-real-time  
 1270 products, F2 and FM2, show good accuracy, similar to other fused products. Interestingly, the  
 1271 accuracy of F1 was worse than that of F2, but the accuracy of FM1 was better than that of  
 1272 FM2. The reason for this appears that the long-term RMSE (in Figure 1) and Gaussian center  
 1273 value (in Figure 3) was a better representation for the EMERGe than for the KORUS-AQ  
 1274 period. To minimize such errors, overall results can be improved by binning the RMSE and  
 1275 Gaussian center value for the bias correction with respect to month and season in addition to  
 1276 NDVI and time. Naturally, if we directly use the RMSE and Gaussian center value of each  
 1277 campaign, the accuracy can be improved.  
 1278 In terms of %GCOS range, satellite-derived and fused products was 33-43% and 46-54%,  
 1279 respectively during the KORUS-AQ, indicating that the fused products have a better or  
 1280 similar statistical score along with other validation scores such as RMSE and MBE. However,  
 1281 the %GCOS during the EMERGe period shows better accuracy for AMR products with 52.4%  
 1282 than for fused products with a maximum of 47.6%. In terms of other validation indices,  
 1283 however, such as RMSE and MBE, the fused product results represent a better validation  
 1284 score than the AMR. For low aerosol loading case where RMSE is small and similar across  
 1285 different products, bias correction effect was also analyzed at the Gangneung-WNU site by  
 1286 comparing F3 and FM3.  
 1287 As a summary, to increase the accuracy of the fused products, it is required to have either  
 1288 high accuracy of the respective satellite product, or the consistent error characteristics with  
 1289 respect to different parameters such as time, NDVI, etc. If either each satellite-derived AOD,  
 1290 is accurate or large numbers of ensemble members are available for compensating respective  
 1291 error, the ensemble-mean shall be the better fusion technique. If the error characteristic is not  
 1292 random and can be expressed as a specific function, the fused product's accuracy through the  
 1293 MLE fusion will be increased.  
 1294 The method applied in this study could be used for AOD fusion of GEO data, such as AMI  
 1295 onboard GK-2A, GOCI-2 and GEMS onboard GK-2B. Furthermore, it is possible to retrieve  
 1296 AOPs other than AOD using multi-angle and multi-channel (UV, VIS, and IR) observations  
 1297 with GK-2A and 2B.

1300 **Code and data availability.**

1301 The aerosol products data from AHI and GOCI are available on request from the  
 1302 corresponding author (jkim2@yonsei.ac.kr).  
 1303  
 1304

삭제함: , as well as MLE products, including pixel-level err [... [27]

삭제함: The accuracy after fusion was better than that of individual satellite product. The

삭제함: The %EE of each satellite-derived product during the KORUS-AQ was 53.2%, 58.0%, 52.2%, and 50.3% in AMR, AES, GV1, and GV2; and the RMSE was 0.180, 0.201, 0.153, and 0.176, respectively. After the ensemble-mean process, the EE of F1, F2, F3, and F4 increased to 67.8%, 72.3%, 63.5%, and 73.3%, respectively. FM1, FM2, and FM3, which are results of MLE fusion, had %EE values of 71.5%, 65.6%, and 65.0%, with RMSE values of 0.131, 0.148, and 0.161, respectively, better than the respective satellite product. Similarly, the EMERGe period displayed better statistical values after fusion, with EE and RMSE values of 68.0% and 0.149, respectively.

삭제함: ...orTo...provide ...ptimized AOD products for [... [28]

삭제함: mean and MLE fusion [... [29]

삭제함: , and both show consistent results

삭제함: , indicating that there is no significant difference from the mean AOD in Figures 4(f) and 5 (f)...

서식 있음: 들여쓰기: 첫 줄: 0 글자

삭제함: due to depending on the number of ensemble ...embd [... [30]

삭제함: However, since both satellite algorithms retrieved AOPs through VIS channels, there remains an issue of reduced accuracy over brighter surfaces, with AOP retrieval in the VIS channel being more accurate over dark surfaces, and with results being more

삭제함: ace

삭제함: s, and with results being more accurate during the KORUS-AQ period than the EMERGe period. The fus

삭제함: The fusion products improved the accuracy of satellite products, and MLE products also improved the accuracy by taking into account pixel-based errors based on long-term data analysis. The range of %GCOS range, of ...atellite-derived products ... [31]

서식 있음: 들여쓰기: 첫 줄: 1 글자

삭제함: In addition... methods ...o increase the accuracy of [... [32]

삭제함: and

삭제함: .

1436 **Author contributions.**

1437  
1438 HL, SG and JK designed the experiment. HL and SG carried out the data processing. MC, SL,  
1439 and YK provided support on satellite data. HL wrote the manuscript with contributions from  
1440 co-authors. JK reviewed and edited the article. JK and CK provided support and supervision.  
1441 All authors analyzed the measurement data and prepared the article with contributions from  
1442 all co-authors.

1443  
1444 **Competing interests.**

1445  
1446 The authors declare that they have no conflict of interest.  
1447

1448 **Acknowledgements**

1449 We thank all principal investigators and their staff for establishing and maintaining the  
1450 AERONET sites used in this investigation. This subject is supported by Korea Ministry of  
1451 Environment (MOE) as "Public Technology Program based on Environmental Policy  
1452 (2017000160001)". This work was also supported by a grant from the National Institute of  
1453 Environment Research (NIER), funded by the Ministry of Environment (MOE) of the  
1454 Republic of Korea (NIER-2020-01-02-007). This research was also supported by the National  
1455 Strategic Project-Fine particle of the National Research Foundation of Korea (NRF) funded  
1456 by the Ministry of Science and ICT (MSIT), the Ministry of Environment (ME), and the  
1457 Ministry of Health and Welfare (MOHW) (NRF-2017M3D8A1092022). We thank all  
1458 members of the KORUS-AQ science team for their contributions to the field study and the  
1459 data processing (doi:10.5067/Suborbital/KORUSAQ/DATA01).  
1460

1461 **References**

- 1462 Bernard, E., Moulin, C., Ramon, D., Jolivet, D., Riedi, J., and Nicolas, J. M.: Description and validation of an  
1463 AOT product over land at the 0.6  $\mu\text{m}$  channel of the SEVIRI sensor onboard MSG, *Atmospheric Measurement*  
1464 *Techniques*, 4, 2543-2565, 2011.
- 1465 Bessho, K., Date, K., Hayashi, M., Ikeda, A., Imai, T., Inoue, H., Kumagai, Y., Miyakawa, T., Murata, H., Ohno,  
1466 T., Okuyama, A., Oyama, R., Sasaki, Y., Shimazu, Y., Shimoji, K., Sumida, Y., Suzuki, M., Taniguchi, H.,  
1467 Tsuchiyama, H., Uesawa, D., Yokota, H., and Yoshida, R.: An Introduction to Himawari-8/9&mdash;  
1468 Japan&rsquo;s New-Generation Geostationary Meteorological Satellites, *Journal of the Meteorological Society*  
1469 *of Japan*. Ser. II, 94, 151-183, 2016.
- 1470 Bilal, M., Nichol, J. E., and Wang, L.: New customized methods for improvement of the MODIS C6 Dark  
1471 Target and Deep Blue merged aerosol product, *Remote Sensing of Environment*, 197, 115-124, 2017.
- 1472 Chatterjee, A., Michalak, A. M., Kahn, R. A., Paradise, S. R., Braverman, A. J., and Miller, C. E.: A  
1473 geostatistical data fusion technique for merging remote sensing and ground-based observations of aerosol  
1474 optical thickness, *Journal of Geophysical Research*, 115, 2010.
- 1475 Cho, Hi K., Jeong, M. J., Kim, J., Kim, Y. J.: Dependence of diffuse photosynthetically active solar irradiance  
1476 on total optical depth, *Journal of Geophysical Research*, 108, D9, 4267, 4-1-4-10, 2003.  
1477

서식 지정합: 글꼴: 12 pt

1478 Choi, J.-K., Park, Y. J., Ahn, J. H., Lim, H.-S., Eom, J., and Ryu, J.-H.: GOCI, the world's first geostationary  
1479 ocean color observation satellite, for the monitoring of temporal variability in coastal water turbidity, *Journal of*  
1480 *Geophysical Research: Oceans*, 117, C9, 2012.

1481 Choi, M., Kim, J., Lee, J., Kim, M., Park, Y.-J., Jeong, U., Kim, W., Hong, H., Holben, B. N., Eck, T. F., Song,  
1482 C. H., Lim, J.-H., and Song, C.-K.: GOCI Yonsei Aerosol Retrieval (YAER) algorithm and validation during  
1483 the DRAGON-NE Asia 2012 campaign, *Atmos. Meas. Tech.*, 9, 1377-1398, 2016.

1484 Choi, M., Kim, J., Lee, J., Kim, M., Park, Y.-J., Holben, B., Eck, T. F., Li, Z., and Song, C. H.: GOCI Yonsei  
1485 aerosol retrieval version 2 products: an improved algorithm and error analysis with uncertainty estimation from  
1486 5-year validation over East Asia, *Atmospheric Measurement Techniques*, 11, 385-408, 2018.

1487 Cox, C.: Statistics of the sea surface derived from sun glitter, *J. Marine Research*, 13, 198-227, 1954.

1488 [Crawford, J. J.-Y., Ahn, J. Al-Saadi, L. Chang, L. K. Emmons, J. Kim, G. Lee, J.-H. Park, R. J. Park, J. H. Woo,](#)  
1489 [C.-K. Song, J.-H. Hong, Y.-D. Hong, B. L. Lefer, M. Lee, T. Lee, S. Kim, K.-E. Min, S. S. Yum, H. J. Shin, Y.-](#)  
1490 [W. Kim, J.-S. Choi, J.-S. Park, J. J. Szykman, R. W. Long, C. E. Jordan, I. J. Simpson, A. Fried, J. E. Dibb, S. Y.](#)  
1491 [Cho, and Y. P. Kim; The Korea-United States Air Quality \(KORUS-AQ\) Field Study, Elementa, revised, 2021.](#)  
1492

1493 Fukuda, S., Nakajima, T., Takenaka, H., Higurashi, A., Kikuchi, N., Nakajima, T. Y., and Ishida, H.: New  
1494 approaches to removing cloud shadows and evaluating the 380 nm surface reflectance for improved aerosol  
1495 optical thickness retrievals from the GOSAT/TANSO-Cloud and Aerosol Imager, *Journal of Geophysical*  
1496 *Research: Atmospheres*, 118, 13, 520-513, 531, 2013.

1497 Garay, M. J., Kalashnikova, O. V., and Bull, M. A.: Development and assessment of a higher-spatial-resolution  
1498 (4.4 km) MISR aerosol optical depth product using AERONET-DRAGON data, *Atmospheric Chemistry and*  
1499 *Physics*, 17, 5095-5106, 2017.

1500 Garay, M. J., Witek, M. L., Kahn, R. A., Seidel, F. C., Limbacher, J. A., Bull, M. A., Diner, D. J., Hansen, E. G.,  
1501 Kalashnikova, O. V., Lee, H., Nastan, A. M., and Yu, Y.: Introducing the 4.4&#8201;km spatial resolution  
1502 Multi-Angle Imaging SpectroRadiometer (MISR) aerosol product, *Atmospheric Measurement Techniques*, 13,  
1503 593-628, 2020.

1504 [GCOS, W.: Systematic Observation Requirements for Satellite-BASED Data Products for Climate, 154](#)  
1505 [Document, 2011.](#)

1506

1507 Giles, D. M., Sinyuk, A., Sorokin, M. S., Schafer, J. S., Smirnov, A., Slutsker, I., Eck, T. F., Holben, B. N.,  
1508 Lewis, J., Campbell, J., Welton, E. J., Korkin, S., and Lyapustin, A.: Advancements in the Aerosol Robotic  
1509 Network (AERONET) Version 3 Database – Automated Near Real-Time Quality Control Algorithm with  
1510 Improved Cloud Screening for Sun Photometer Aerosol Optical Depth (AOD) Measurements, *Atmos. Meas.*  
1511 *Tech. Discuss.*, doi: <https://doi.org/10.5194/amt-2018-272>, 2018. 2018.

1512 Go, S., Kim, J., Park, S. S., Kim, M., Lim, H., Kim, J.-Y., Lee, D.-W., and Im, J.: Synergistic Use of  
1513 Hyperspectral UV-Visible OMI and Broadband Meteorological Imager MODIS Data for a Merged Aerosol  
1514 Product, *Remote Sensing*, 12, 2020.

1515

1516 Gupta, P., Patadia, F., and Christopher, S. A.: Multisensor Data Product Fusion for Aerosol Research, *IEEE*  
1517 *Transactions on Geoscience and Remote Sensing*, 46, 1407-1415, 2008.

1518 Gupta, P., Levy, R. C., Mattoo, S., Remer, L. A., and Munchak, L. A.: A surface reflectance scheme for  
1519 retrieving aerosol optical depth over urban surfaces in MODIS Dark Target retrieval algorithm, *Atmospheric*  
1520 *Measurement Techniques*, 9, 3293-3308, 2016.

1521 Gupta, P., Levy, R. C., Mattoo, S., Remer, L. A., Holz, R. E., and Heidinger, A. K.: Applying the Dark Target  
1522 aerosol algorithm with Advanced Himawari Imager observations during the KORUS-AQ field campaign, 2019.  
1523

1524 Herman, J., Bhartia, P., Torres, O., Hsu, C., Seftor, C., and Celarier, E.: Global distribution of UV-absorbing  
1525 aerosols from Nimbus 7/TOMS data, *Journal of Geophysical Research: Atmospheres*, 102, 16911-16922, 1997.

서식 지정함: 글꼴: 10 pt  
서식 지정함: 글꼴: 10 pt  
서식 지정함: 글꼴: 10 pt  
서식 지정함: 글꼴: 10 pt, 영어(미국)  
서식 지정함: 글꼴: (영어) Times New Roman, 굵게  
서식 있음: 표준

서식 있음: 표준  
삭제함: cos  
서식 지정함: 글꼴: 10 pt, 영어(영국)  
서식 지정함: 글꼴: 10 pt  
서식 지정함: 글꼴: (영어) Times New Roman, (한글) 바탕, 12 pt, 굵게, (한글) 한국어

1527 Holben, B. N., Tanre, D., Smirnov, A., Eck, T., Slutsker, I., Abuhassan, N., Newcomb, W., Schafer, J., Chatenet,  
1528 B., and Lavenu, F. J. J. o. G. R. A.: An emerging ground-based aerosol climatology: Aerosol optical depth from  
1529 AERONET, 106, 12067-12097, 2001.

1530 Hsu, N. C., Tsay, S.-C., King, M. D., Herman, J. R. J. I. T. o. G., and Sensing, R.: Aerosol properties over  
1531 bright-reflecting source regions, 42, 557-569, 2004.

1532 Hsu, N., Jeong, M. J., Bettenhausen, C., Sayer, A., Hansell, R., Seftor, C., Huang, J., and Tsay, S. C.: Enhanced  
1533 Deep Blue aerosol retrieval algorithm: The second generation, *Journal of Geophysical Research: Atmospheres*,  
1534 118, 9296-9315, 2013.

1535 Hsu, N., Lee, J., Sayer, A., Kim, W., Bettenhausen, C., and Tsay, S. C. J. J. o. G. R. A.: VIIRS Deep Blue  
1536 aerosol products over land: Extending the EOS long-term aerosol data records, 124, 4026-4053, 2019.

1537 Jackson, J. M., Liu, H., Laszlo, I., Kondragunta, S., Remer, L. A., Huang, J., and Huang, H.-C.: Suomi-NPP  
1538 VIIRS aerosol algorithms and data products, *Journal of Geophysical Research: Atmospheres*, 118, 12,673-  
1539 612,689, 2013.

1540 Kikuchi, M., Murakami, H., Suzuki, K., Nagao, T. M., and Higurashi, A.: Improved Hourly Estimates of  
1541 Aerosol Optical Thickness Using Spatiotemporal Variability Derived From Himawari-8 Geostationary Satellite,  
1542 *IEEE Transactions on Geoscience and Remote Sensing*, 56, 3442-3455, 2018.

1543 Kim, J., Lee, J., Lee, H. C., Higurashi, A., Takemura, T., and Song, C. H.: Consistency of the aerosol type  
1544 classification from satellite remote sensing during the Atmospheric Brown Cloud-East Asia Regional  
1545 Experiment campaign, *J. Geophys. Res.*, 112, D22S33, doi:10.1029/2006JD008201, 2007.

1546 Kim, J., Yoon, J. M., Ahn, M. H., Sohn, B. J., and Lim, H. S.: Retrieving aerosol optical depth using visible and  
1547 mid-IR channels from geostationary satellite MTSAT-1R, *International Journal of Remote Sensing*, 29, 6181-  
1548 6192, 2008.

1549 Kim, J., Kim, M., and Choi, M.: Monitoring aerosol properties in east Asia from geostationary orbit: GOCI, MI  
1550 and GEMS. In: *Air Pollution in Eastern Asia: An Integrated Perspective*, Springer, 2017.

1551 Kim, J., Jeong, U., Ahn, M.-H., Kim, J. H., Park, R. J., Lee, H., Song, C. H., Choi, Y.-S., Lee, K.-H., Yoo, J.-M.,  
1552 Jeong, M.-J., Park, S. K., Lee, K.-M., Song, C.-K., Kim, S.-W., Kim, Y. J., Kim, S.-W., Kim, M., Go, S., Liu,  
1553 X., Chance, K., Chan Miller, C., Al-Saadi, J., Veihelmann, B., Bhartia, P. K., Torres, O., Abad, G. G., Haffner,  
1554 D. P., Ko, D. H., Lee, S. H., Woo, J.-H., Chong, H., Park, S. S., Nicks, D., Choi, W. J., Moon, K.-J., Cho, A.,  
1555 Yoon, J., Kim, S.-k., Hong, H., Lee, K., Lee, H., Lee, S., Choi, M., Veefkind, P., Levelt, P. F., Edwards, D. P.,  
1556 Kang, M., Eo, M., Bak, J., Baek, K., Kwon, H.-A., Yang, J., Park, J., Han, K. M., Kim, B.-R., Shin, H.-W., Choi,  
1557 H., Lee, E., Chong, J., Cha, Y., Koo, J.-H., Irie, H., Hayashida, S., Kasai, Y., Kanaya, Y., Liu, C., Lin, J.,  
1558 Crawford, J. H., Carmichael, G. R., Newchurch, M. J., Lefer, B. L., Herman, J. R., Swap, R. J., Lau, A. K. H.,  
1559 Kurosu, T. P., Jaross, G., Ahlers, B., Dobber, M., McElroy, C. T., and Choi, Y.: New Era of Air Quality  
1560 Monitoring from Space: Geostationary Environment Monitoring Spectrometer (GEMS), *Bulletin of the  
1561 American Meteorological Society*, 101, E1-E22, 2020.

1562 Kim, M., Kim, J., Wong, M. S., Yoon, J., Lee, J., Wu, D., Chan, P. W., Nichol, J. E., Chung, C.-Y., and Ou, M.-  
1563 L.: Improvement of aerosol optical depth retrieval over Hong Kong from a geostationary meteorological satellite  
1564 using critical reflectance with background optical depth correction, *Remote Sensing of Environment*, 142, 176-  
1565 187, 2014.

1566 Kim, M., Kim, J., Jeong, U., Kim, W., Hong, H., Holben, B., Eck, T. F., Lim, J. H., Song, C. K., Lee, S., and  
1567 Chung, C. Y.: Aerosol optical properties derived from the DRAGON-NE Asia campaign, and implications for a  
1568 single-channel algorithm to retrieve aerosol optical depth in spring from Meteorological Imager (MI) on-board  
1569 the Communication, Ocean, and Meteorological Satellite (COMS), *Atmos. Chem. Phys.*, 16, 1789-1808, 2016.

1570 Kim, M., Kim, S. H., Kim, W. V., Lee, Y. G., Kim, J., and Kafatos, M. C.: Assessment of Aerosol optical depth  
1571 under background and polluted conditions using AERONET and VIIRS datasets, *Atmospheric Environment*,  
1572 245, 2021.

1573 Knapp, K. R., Frouin, R., Kondragunta, S., and Prados, A.: Toward aerosol optical depth retrievals over land  
1574 from GOES visible radiances: determining surface reflectance, *International Journal of Remote Sensing*, 26,  
1575 4097-4116, 2007.

**삭제함:** Knapp, K. R. J. J. o. G. R. A.: Quantification of aerosol signal in GOES 8 visible imagery over the United States, 107, AAC 4-1-AAC 4-11, 2002.

- 1579 Koelemeijer, R., De Haan, J., and Stammes, P.: A database of spectral surface reflectivity in the range 335–772  
1580 nm derived from 5.5 years of GOME observations, *Journal of Geophysical Research: Atmospheres*, 108, 2003.
- 1581 Lee, J., Kim, J., Song, C. H., Ryu, J.-H., Ahn, Y.-H., and Song, C.: Algorithm for retrieval of aerosol optical  
1582 properties over the ocean from the Geostationary Ocean Color Imager, *Remote Sensing of Environment*, 114,  
1583 1077-1088, 2010.
- 1584 Lee, J., Kim, J., Yang, P., and Hsu, N. C.: Improvement of aerosol optical depth retrieval from MODIS spectral  
1585 reflectance over the global ocean using new aerosol models archived from AERONET inversion data and tri-  
1586 axial ellipsoidal dust database, *Atmospheric Chemistry and Physics*, 12, 7087-7102, 2012.
- 1587 Levy, R. C., Remer, L. A., Kleidman, R. G., Mattoo, S., Ichoku, C., Kahn, R., and Eck, T. F.: Global evaluation  
1588 of the Collection 5 MODIS dark-target aerosol products over land, *Atmospheric Chemistry and Physics*, 10,  
1589 10399-10420, 2010.
- 1590 Levy, R. C., Mattoo, S., Munchak, L. A., Remer, L. A., Sayer, A. M., Patadia, F., and Hsu, N. C.: The  
1591 Collection 6 MODIS aerosol products over land and ocean, *Atmospheric Measurement Techniques*, 6, 2989-  
1592 3034, 2013.
- 1593 Lee, S., Kim, M., Choi, M., Go, S., Kim, J., Kim, J.-H., Lim, H.-K., Jeong, U., Goo, T.-Y., Kuze, A., Shiomi, K.,  
1594 and Tatsuya, Y.: Aerosol Property Retrieval Algorithm over Northeast Asia from TANSO-CAI Measurements  
1595 Onboard GOSAT, *Remote Sensing*, 9, 2017.
- 1596 Lee, S., Kim, J., Choi, M., Hong, J., Lim, H., Eck, T. F., Holben, B. N., Ahn, J.-Y., Kim, J., and Koo, J.-H.:  
1597 Analysis of long-range transboundary transport (LRTT) effect on Korean aerosol pollution during the KORUS-  
1598 AQ campaign, *Atmospheric Environment*, 204, 53-67, 2019.
- 1599 Li, L., Shi, R., Zhang, L., Zhang, J., and Gao, W.: The data fusion of aerosol optical thickness using universal  
1600 kriging and stepwise regression in East China, 2014, 922112.
- 1603 Lim, H., Choi, M., Kim, M., Kim, J., and Chan, P. W.: Retrieval and Validation of Aerosol Optical Properties  
1604 Using Japanese Next Generation Meteorological Satellite, Himawari-8, *Korean Journal of Remote Sensing*, 32,  
1605 681-691, 2016.
- 1606 Lim, H., Choi, M., Kim, J., Kasai, Y., and Chan, P.: AHI/Himawari-8 Yonsei Aerosol Retrieval (YAER):  
1607 Algorithm, Validation and Merged Products, *Remote Sens.*, 10, 2018.
- 1608 Lyapustin, A., Martonchik, J., Wang, Y., Laszlo, I., and Korkin, S.: Multiangle implementation of atmospheric  
1609 correction (MAIAC): 1. Radiative transfer basis and look-up tables, *Journal of Geophysical Research*, 116,  
1610 2011a.
- 1611 Lyapustin, A., Wang, Y., Laszlo, I., Kahn, R., Korkin, S., Remer, L., Levy, R., and Reid, J. S.: Multiangle  
1612 implementation of atmospheric correction (MAIAC): 2. Aerosol algorithm, *Journal of Geophysical Research*,  
1613 116, 2011b.
- 1614 Lyapustin, A., Wang, Y., Korkin, S., and Huang, D.: MODIS Collection 6 MAIAC algorithm, *Atmospheric  
1615 Measurement Techniques*, 11, 5741-5765, 2018.
- 1616 Mélin, F., Zibordi, G., and Djavidnia, S.: Development and validation of a technique for merging satellite  
1617 derived aerosol optical depth from SeaWiFS and MODIS, *Remote Sensing of Environment*, 108, 436-450, 2007.
- 1618 Murakami, H.: Ocean color estimation by Himawari-8/AHI, 2016, 987810.
- 1619 Negi, H. and Kokhanovsky, A. J. T. C.: Retrieval of snow albedo and grain size using reflectance measurements  
1620 in Himalayan basin, 5, 203, 2011.
- 1621 Nguyen, H., Cressie, N., and Braverman, A.: Spatial Statistical Data Fusion for Remote Sensing Applications,  
1622 *Journal of the American Statistical Association*, 107, 1004-1018, 2012.
- 1623 Nirala, M.: Technical Note: Multi-sensor data fusion of aerosol optical thickness, *International Journal of  
1624 Remote Sensing*, 29, 2127-2136, 2008.

1625 Pang, J., Liu, Z., Wang, X., Bresch, J., Ban, J., Chen, D., and Kim, J.: Assimilating AOD retrievals from GOCI  
1626 and VIIRS to forecast surface PM2.5 episodes over Eastern China, *Atmospheric Environment*, 179, 288-304,  
1627 2018.

1628 Remer, L. A., Kaufman, Y., Tarré, D., Mattoo, S., Chu, D., Martins, J. V., Li, R.-R., Ichoku, C., Levy, R., and  
1629 Kleidman, R.: The MODIS aerosol algorithm, products, and validation, *Journal of the atmospheric sciences*, 62,  
1630 947-973, 2005.

1631 Remer, L. A., Mattoo, S., Levy, R. C., and Munchak, L.: MODIS 3 km aerosol product: algorithm and global  
1632 perspective, *Atmospheric Measurement Techniques Discussions*, 6, 69-112, 2013.

1633 Saide, P. E., Kim, J., Song, C. H., Choi, M., Cheng, Y., and Carmichael, G. R.: Assimilation of next generation  
1634 geostationary aerosol optical depth retrievals to improve air quality simulations, *Geophysical Research Letters*,  
1635 41, 9188-9196, 2014.

1636 Saide, P. E., Gao, M., Lu, Z., Goldberg, D., Streets, D. G., Woo, J.-H., Beyersdorf, A., Corr, C. A., Thornhill, K.  
1637 L., Anderson, B., Hair, J. W., Nehrir, A. R., Diskin, G. S., Jimenez, J. L., Nault, B. A., Campuzano-Jost, P.,  
1638 Dibb, J., Heim, E., Lamb, K. D., Schwarz, J. P., Perring, A. E., Kim, J., Choi, M., Holben, B., Pfister, G.,  
1639 Hodzic, A., Carmichael, G. R., Emmons, L., and Crawford, J. H. : Understanding and improving model  
1640 representation of aerosol optical properties for a Chinese haze event measured during KORUS-AQ,  
1641 *Atmospheric Chemistry and Physics*, 20, 6455-6478, 2020.

1642  
1643 Sayer, A., Munchak, L., Hsu, N., Levy, R., Bettenhausen, C., and Jeong, M. J.: MODIS Collection 6 aerosol  
1644 products: Comparison between Aqua's e-Deep Blue, Dark Target, and "merged" data sets, and usage  
1645 recommendations, *Journal of Geophysical Research: Atmospheres*, 119, 2014.

1646 Sayer, A., Hsu, N., Lee, J., Bettenhausen, C., Kim, W., and Smirnov, A. J. J. o. G. R. A.: Satellite Ocean  
1647 Aerosol Retrieval (SOAR) Algorithm Extension to S-NPP VIIRS as Part of the "Deep Blue" Aerosol Project,  
1648 123, 380-400, 2018.

1649 Sayer, A. M., Hsu, N. C., Lee, J., Kim, W. V., and Dutcher, S. T.: Validation, Stability, and Consistency of  
1650 MODIS Collection 6.1 and VIIRS Version 1 Deep Blue Aerosol Data Over Land, *Journal of Geophysical  
1651 Research: Atmospheres*, 124, 4658-4688, 2019.

1652 Smirnov, A., Holben, B. N., Eck, T. F., Dubovik, O., and Slutsker, I.: Cloud screening and quality control  
1653 algorithms for the AERONET data base, *Remote Sens. Environ.*, 73, 337-349, 2000.

1654 Stocker, T. F., Qin, D., Plattner, G.-K., Tignor, M., Allen, S. K., Boschung, J., Nauels, A., Xia, Y., Bex, B., and  
1655 Midgley, B.: IPCC, 2013: climate change 2013: the physical science basis. Contribution of working group I to  
1656 the fifth assessment report of the intergovernmental panel on climate change. Cambridge University Press, 2013.

1657 Tang, Q., Bo, Y., and Zhu, Y.: Spatiotemporal fusion of multiple-satellite aerosol optical depth (AOD) products  
1658 using Bayesian maximum entropy method, *Journal of Geophysical Research: Atmospheres*, 121, 4034-4048,  
1659 2016.

1660 Wang, J.: Geostationary satellite retrievals of aerosol optical thickness during ACE-Asia, *Journal of  
1661 Geophysical Research*, 108, 2003.

1662 Wang, J., Brown, D. G., and Hammerling, D.: Geostatistical inverse modeling for super-resolution mapping of  
1663 continuous spatial processes, *Remote Sensing of Environment*, 139, 205-215, 2013.

1664 Wei, J., Li, Z., Sun, L., Peng, Y., and Wang, L.: Improved merge schemes for MODIS Collection 6.1 Dark  
1665 Target and Deep Blue combined aerosol products, *Atmospheric Environment*, 202, 315-327, 2019. Xie, Y., Xue,  
1666 Y., Che, Y., Guang, J., Mei, L., Voorhis, D., Fan, C., She, L., Xu, H. J. I. T. o. G., and Sensing, R.: Ensemble of  
1667 ESA/AATSR aerosol optical depth products based on the likelihood estimate method with uncertainties, 56,  
1668 997-1007, 2018.

1669 Xu, H., Guang, J., Xue, Y., De Leeuw, G., Che, Y., Guo, J., He, X., and Wang, T. J. A. E.: A consistent aerosol  
1670 optical depth (AOD) dataset over mainland China by integration of several AOD products, 114, 48-56, 2015.

**삭제함:** Sayer, A. M., Hsu, N. C., Bettenhausen, C., and Jeong, M. J.: Validation and uncertainty estimates for MODIS Collection 6 "Deep Blue" aerosol data, *Journal of Geophysical Research: Atmospheres*, 118, 7864-7872, 2013.

1675 Xue, Y., Xu, H., Mei, L., Guang, J., Guo, J., Li, Y., Hou, T., Li, C., Yang, L., He, X. J. A. C., and Discussions,  
1676 P.: Merging aerosol optical depth data from multiple satellite missions to view agricultural biomass burning in  
1677 Central and East China, 12, 10461-10492, 2012.

1678

1679 Yoon, J. M., Kim, J., Lee, J. H., Cho, H. K., Sohn, B.-J., and Ahn, M.-H. J. A.-P. J. o. A. S.: Retrieval of aerosol  
1680 optical depth over East Asia from a geostationary satellite, MTSAT-1R, 43, 49-58, 2007.

1681 Yoshida, M., Kikuchi, M., Nagao, T. M., Murakami, H., Nomaki, T., and Higurashi, A.: Common Retrieval of  
1682 Aerosol Properties for Imaging Satellite Sensors, Journal of the Meteorological Society of Japan. Ser. II, 96B,  
1683 193-209, 2018.

1684 Zhong, G., Wang, X., Tani, H., Guo, M., Chittenden, A., Yin, S., Sun, Z., and Matsumura, S.: A Modified  
1685 Aerosol Free Vegetation Index Algorithm for Aerosol Optical Depth Retrieval Using GOSAT TANSO-CAI  
1686 Data, Remote Sensing, 8, 2016.

1687

1688  
1689

Table 1. Satellite dataset used for the fusion products. [Four entries F1-F4, and three entries FM1-FM3 represent ensemble-mean fusion and MLE fusion products.](#)

AOD type	F1	F2	F3	F4	FM1	FM2	FM3
AER	o	o	o	o	o	o	o
AMR	o		o	o	o		o
GV1	o				o		
GV2	o	o		o	o	o	
Remark	All available products	For NRT <sup>1</sup>	AHI only for wider area	Without GV1 to check missing effect	Same as F1	Same as F2	Same as F3

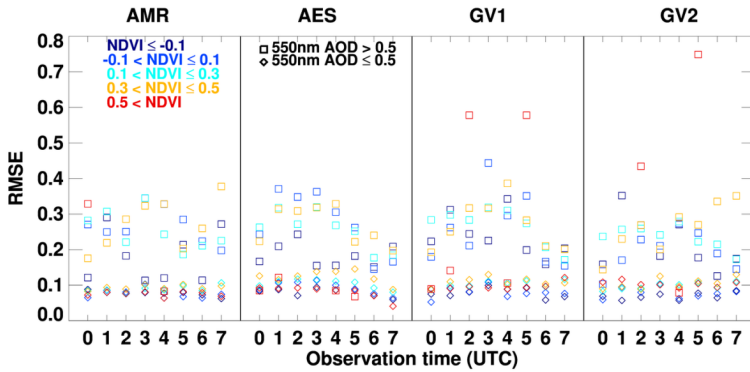
<sup>1</sup> NRT: near real time; <sup>2</sup> Maximum Likelihood Estimation

1690  
1691

서식 지정함: 글꼴: (한글) 바탕, (한글) 한국어

서식 지정함: 글꼴: 10 pt

1692  
1693  
1694



삭제함: [33]

[1] 아래로 이동함: Figure 1. RMSE according to NDVI (color), observation time, and satellite AODs (square and diamond represent AOD at 550nm greater and less equal than 0.5) during Apr. 2018 to Mar. 2019 excluding EMeRGe campaign.

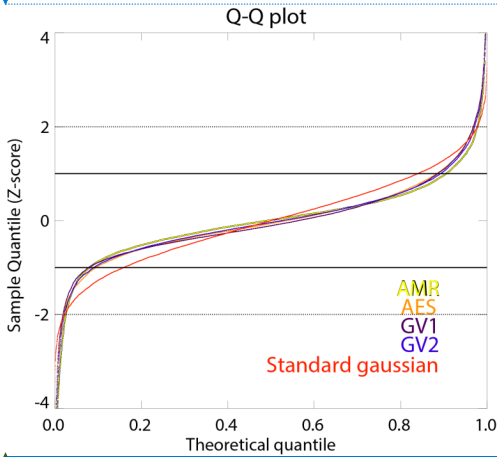
서식 있음: 다음 단락과의 사이에 페이지 나누지 않음

1695  
1696  
1697  
1698

Figure 1. RMSE according to NDVI (color), observation time, and satellite AODs (square and diamond represent AOD at 550nm greater and less equal than 0.5) during Apr. 2018 to Mar. 2019 excluding EMeRGe campaign.

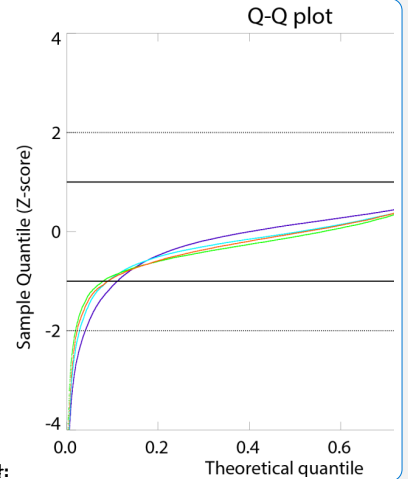
[1] 이동함(삽입)

1699  
1700



삭제함: 구역 나누기(다음 페이지부터)

서식 지정함: 글꼴: (한글) 바탕, (한글) 한국어, (영어2) 영어(영국)



1701  
1702  
1703

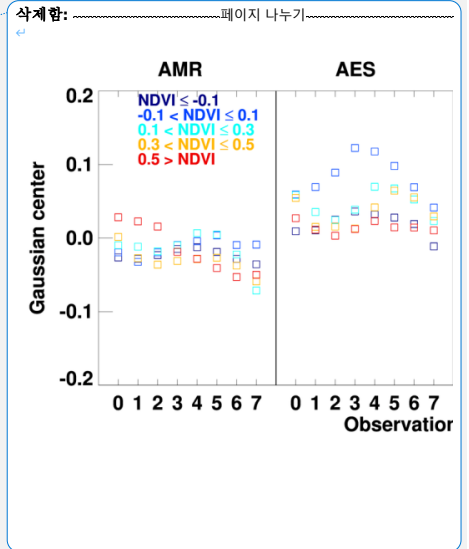
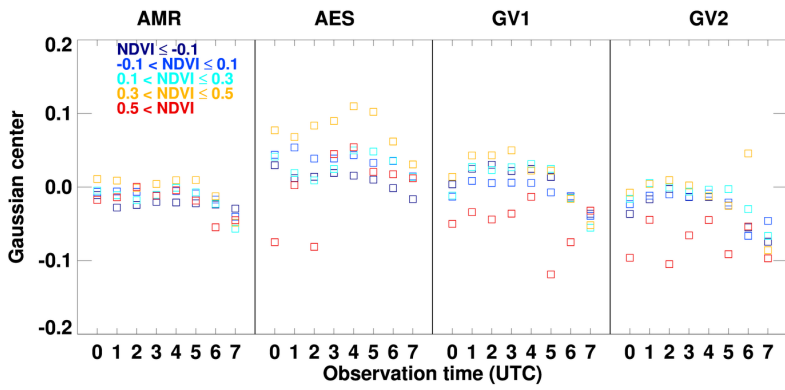
Figure 2. Q-Q plot for the difference between AERONET AOD and AMR(purple), AES(cyan), GV1(green), and GV2(orange) AOD. The black solid line and dotted line represent 1- $\sigma$  and 2- $\sigma$ , respectively.

삭제함:

[2] 아래로 이동함: Figure 2. Q-Q plot for the difference between AERONET AOD and AMR(purple), AES(cyan), GV1(green), and GV2(orange) AOD. The black solid line and dotted line represent 1- $\sigma$  and 2- $\sigma$ , respectively.

[2] 이동함(삽입)

1717



1718

1719

1720

Figure 3. Systematic bias-correction values for NDVI groups and temporal bins for each satellite product from Gaussian fitting analysis used in MLE fusion.

1721

1722

[3] 아래로 이동함: Figure 3. Systematic bias-correction values for NDVI groups and temporal bins for each satellite product from Gaussian fitting analysis used in MLE fusion.

[3] 이동함(삽입)

1729  
1730

Table 2. Validation statistics of the respective satellite product during the KORUS-AQ and the EMeRGe campaign.

Product type	KORUS-AQ					EMeRGe				
	%EE	%GCOS	RMSE	MBE	N	%EE	%GCOS	RMSE	MBE	N
AES	63.5	43.6	0.145	0.029	5069	65.2	46.3	0.176	-0.011	1884
AMR	60.6	39.4	0.150	-0.054	5069	69.4	52.4	0.162	-0.028	1884
GV1	52.2	34.7	0.153	-0.045	4843	63.4	42.7	0.162	-0.035	1760
GV2	50.3	33.8	0.176	0.008	4924	61.5	41.8	0.164	-0.001	1863

1731  
1732

- 서식 지정함: 글꼴: 10 pt, 굵게 없음
- 삭제함: (left)
- 서식 있음: 캡션, 다음 단락과의 사이에 페이지 나누지 않음
- 삭제함: 2
- 삭제함: (right)
- 서식 지정함: 글꼴: (한글) 바탕, 10 pt, (한글) 한국어



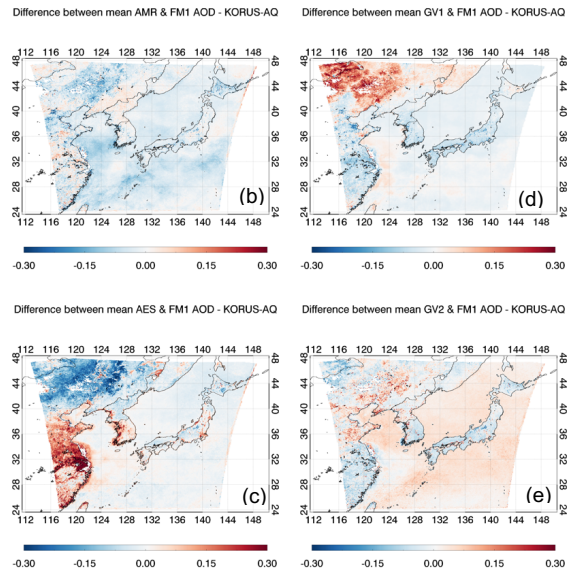
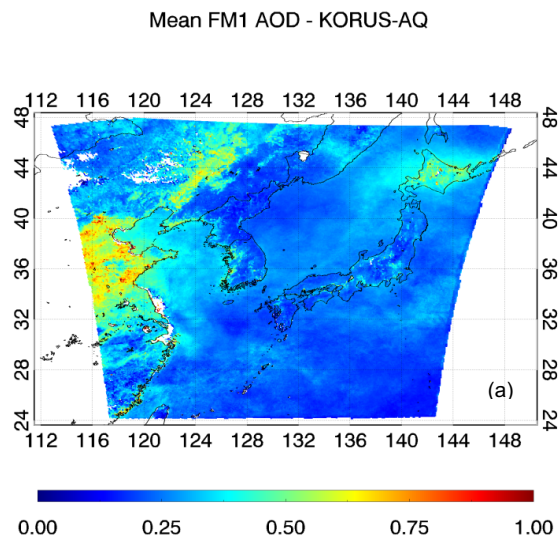


Figure 4. The average AOD of (a) FM1 (AMR, AES, GV1, and GV2) during the KORUS AQ. The difference of mean (b)AMR, (c)AES, (d)GV1, and (e)GV2 AODs with respect to mean representative (FM1) AOD. Figures generated with Interactive Data Language (IDL) version 8.8.0.

서식 있음: 캡션

삭제함: <개방>

삭제함: Figure 5. Same as Figure 4, but for EMeRGe campaign

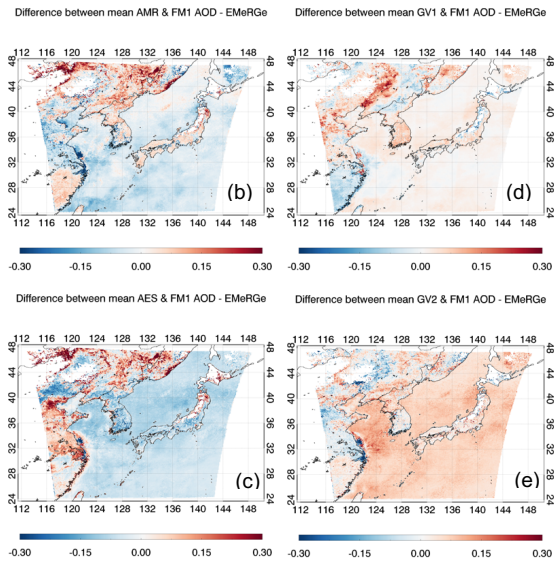
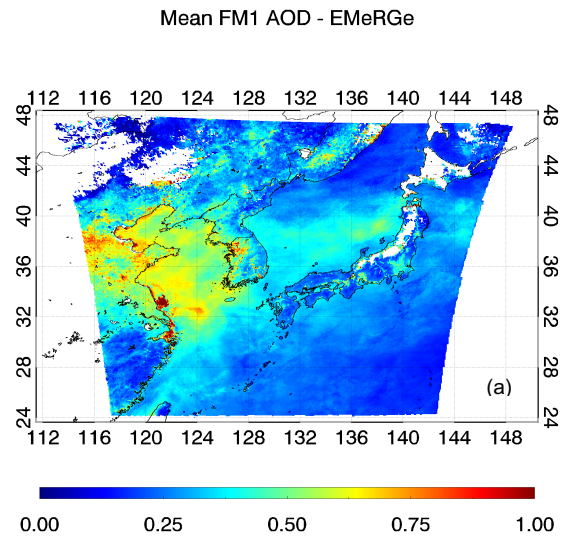


Figure 5. Same as Figure 4, but for EMeRGe campaign.

서식 있음: 캡션

삭제함: <개제><개제>

삭제함: Figure 6. Time series of the AODs at Gangneung WNU site during the KORUS-AQ campaign from (a) respective satellite, (b) ensemble-mean, and (c) MLE fusion (to the right y-axis). Solid line represents difference of individual satellite retrieval from AERONET AOD at 550nm (to the left y-axis)....

5 Table 3. Validation statistics of the ensemble-mean fusion (F1-F4), and MLE fusion (FM1-FM4) AOD during two field campaigns (left: KORUS-AQ, right: EMerGe).

Fusion method	Product type	KORUS-AQ					EMerGe				
		%EE	%GCOS	RMSE	MBE	N	%EE	%GCOS	RMSE	MBE	N
Ensemble-mean	F1	67.8	47.2	0.134	-0.014	4806	66.8	45.4	0.149	-0.012	1754
	F2	72.3	52.7	0.129	0.008	4843	66.9	45.5	0.150	-0.012	1760
	F3	72.1	51.1	0.133	0.012	5069	63.2	44.5	0.175	-0.019	1884
	F4	73.3	51.6	0.128	-0.015	4843	66.4	44.8	0.153	-0.024	1760
MLE	FM1	72.6	52.4	0.130	-0.012	4806	69.1	47.6	0.147	-0.008	1754
	FM2	65.5	46.1	0.146	0.034	4924	67.3	46.5	0.152	0.014	1863
	FM3	75.2	54.5	0.129	-0.09	5069	62.4	41.8	0.177	-0.027	1884

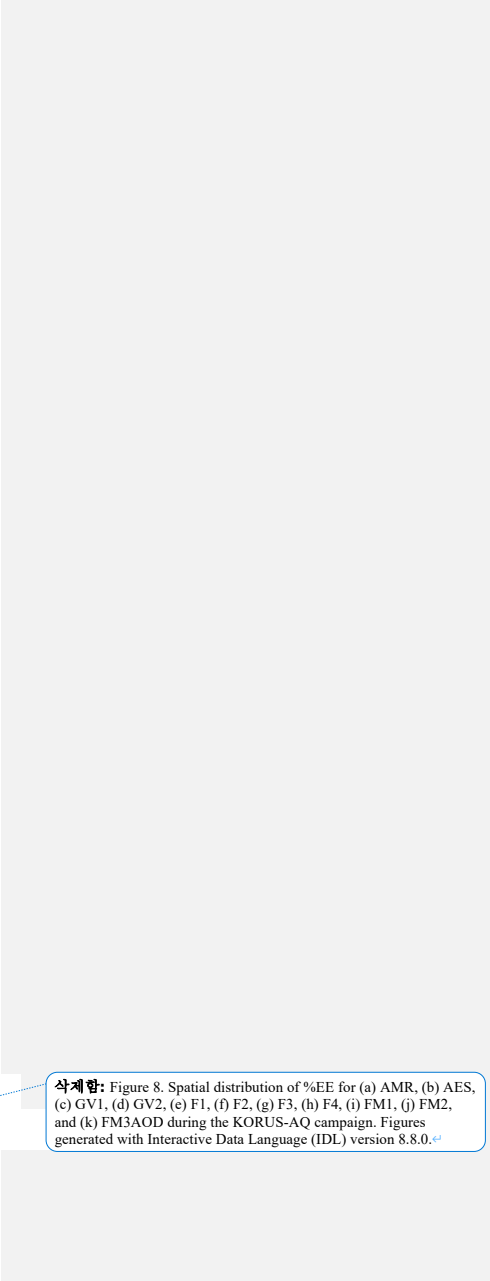
- 삭제함:
- 서식 지정함: 글꼴: 10 pt, 굵게 없음
- 서식 있음: 캡션, 다음 단락과의 사이에 페이지 나누지 않음
- 서식 지정함: 글꼴: (한글) 바탕, 10 pt, (한글) 한국어



Figure 6. Comparison of the GCOS fraction for respective satellite (AMR, AES, GV1, and GV2), ensemble-mean fusion (F1), and MLE fusion (FM1) during the (a) KORUS-AQ and (b) EMeRGe campaign.

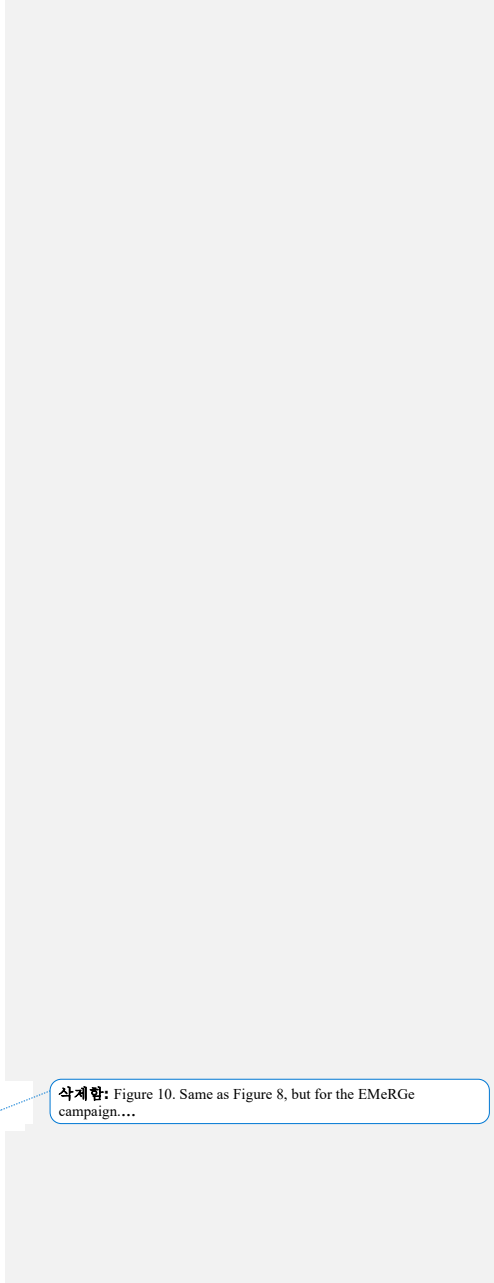
- 서식 지정함: 글꼴: 10 pt, 굵게 없음
- 서식 있음: 캡션
- 서식 지정함: 글꼴: 10 pt, 굵게 없음
- 서식 지정함: 글꼴: 11 pt, (한글) 한국어

삭제함: 



**착제함:** Figure 8. Spatial distribution of %EE for (a) AMR, (b) AES, (c) GV1, (d) GV2, (e) F1, (f) F2, (g) F3, (h) F4, (i) FM1, (j) FM2, and (k) FM3AOD during the KORUS-AQ campaign. Figures generated with Interactive Data Language (IDL) version 8.8.0.

삭제함: Figure 9. Same as Figure 7, but for EMERGe campaign.



삭제함: Figure 10. Same as Figure 8, but for the EMerGe campaign...

25  
30

삭제합:

삭제합: Figure 11. Difference between (a, d) respective, (b, e) ensemble-mean, or (c, f) MLE and AERONET AOD in terms of NDVI during the KORUS-AQ (left column) and the EMeRGe (right column) campaigns. Each points and solid lines represent the median and 1- $\sigma$  (16<sup>th</sup> and 84<sup>th</sup> percentile) of 800 (for the KORUS-AQ) and 600 (for the EMeRGe) collocated data points in terms of NDVI values.<sup>41</sup>

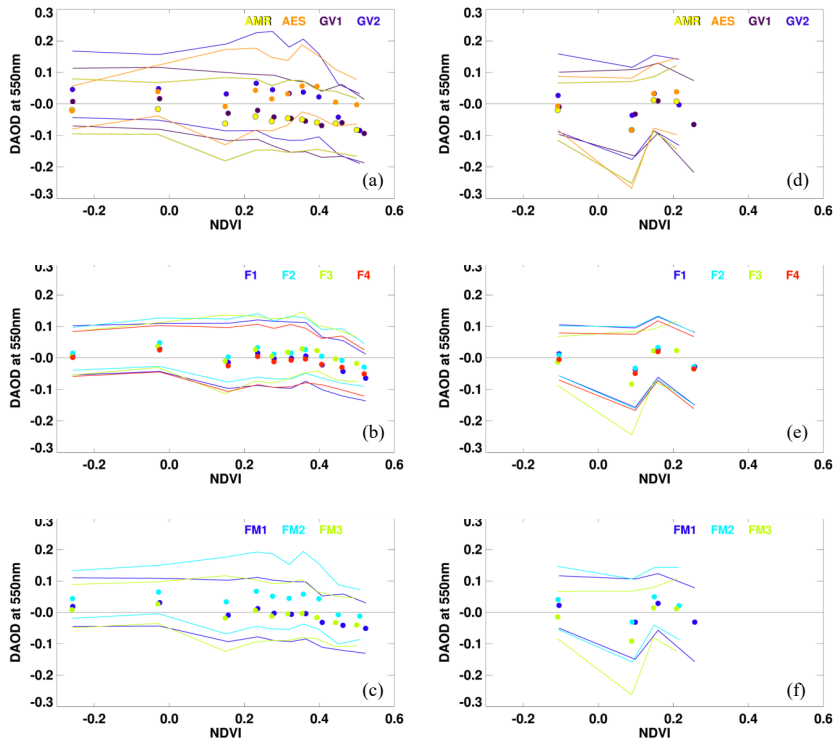


Figure 7. Difference between (a, d) respective, (b, e) ensemble-mean, or (c, f) MLE and AERONET AOD in terms of NDVI during the KORUS-AQ (left column) and the EMeRGe (right column) campaigns. Each point and solid lines represent the median and 1- $\sigma$  (16<sup>th</sup> and 84<sup>th</sup> percentile) of 500 (for the KORUS-AQ) and 400 (for the EMeRGe) collocated data points in terms of NDVI values.

서식 있음: 줄 간격: 1줄, 다음 단락과의 사이에 페이지 나누기

서식 없음: 표준, 줄 간격: 2줄, 다음 단락과의 사이에 페이지 나누지 않음

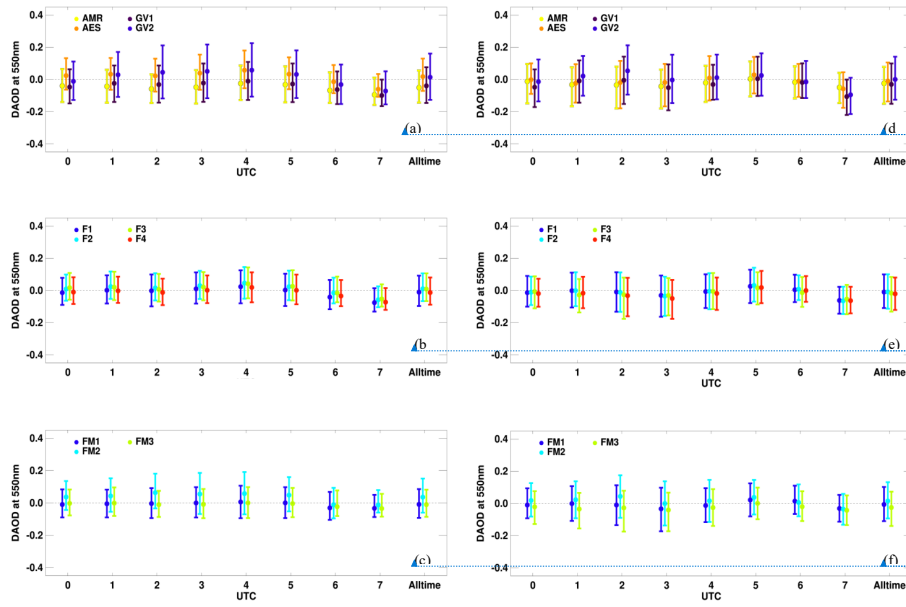
서식 지정함: 글꼴: 10 pt, 굵게 없음

서식 있음: 캡션, 줄 간격: 1줄, 다음 단락과의 사이에 페이지 나누기

서식 지정함: 글꼴: 11 pt, (한글) 한국어

40

삭제함:  
Figure 12. Same as Figure 11, but for the observation time.



서식 지정함: 글꼴: 8 pt  
 서식 지정함: 글꼴: 8 pt

서식 지정함: 글꼴: 8 pt  
 서식 지정함: 글꼴: 8 pt

서식 지정함: 글꼴: 8 pt  
 서식 지정함: 글꼴: 8 pt

Figure 8. Same as Figure8, but for the observation time.

서식 지정함: 글꼴: 10 pt, 굵게 없음  
 서식 지정함: 글꼴: 10 pt, 굵게 없음  
 서식 있음: 캡션

삭제함:

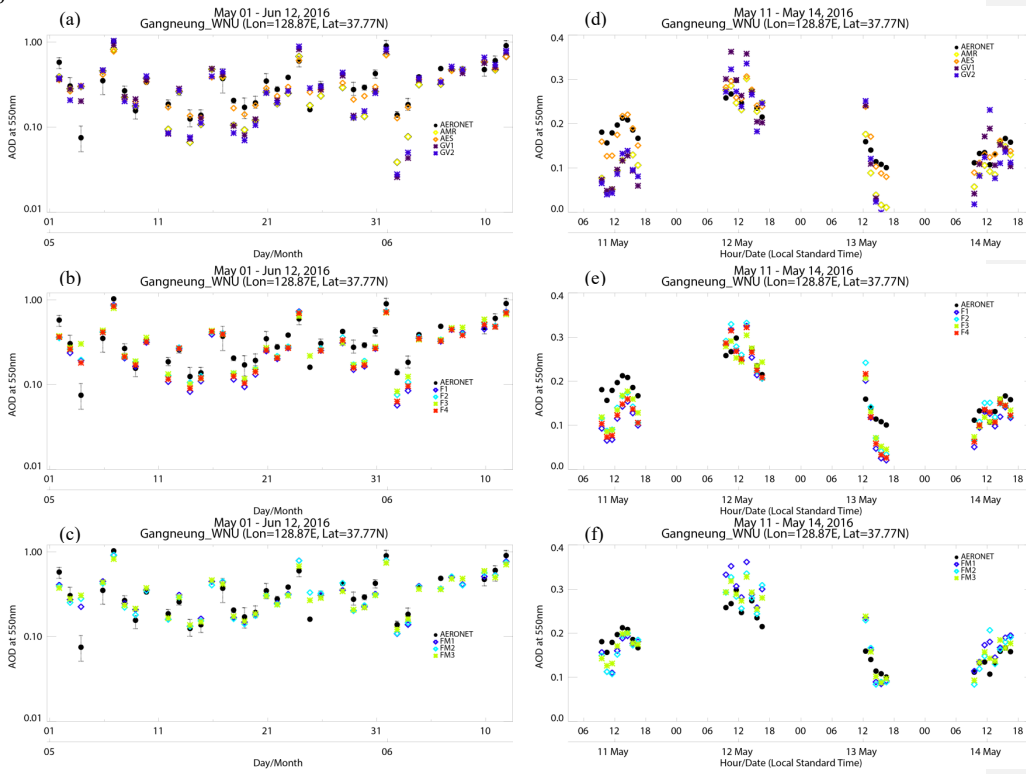


Figure 9. Time series of the daily average AODs at Gangneung WNU site during the KORUS-AQ campaign from (a) respective satellite, (b) ensemble-mean, and (c) MLE fusion. The black-filled circle represents AERONET AOD, and the error bar represents 1-SD of daily AERONET AODs. The diurnal variation in AODs from 11 to 14 May 2016 is shown in the right column, where (d) is the respective satellite, (e) is fused, and (f) is MLE products.

- 서식 있음: 캡션
- 서식 지정함: 글꼴: 10 pt, 굵게 없음
- 서식 지정함: 글꼴: 굵게 없음
- 서식 지정함: 글꼴: 10 pt, (한글) 한국어

Table 4. Accuracy evaluation of outside of GOCI area of AMR, AES, F3, and FM3 AODs.

Without GOCI domain	KORUS-AQ AMR	KORUS-AQ AES	KORUS-AQ F3	KORUS-AQ FM3	EMeRGe AMR	EMeRGe AES	EMeRGe F3	EMeRGe FM3
N	1959	1958	1958	1958	2610	2610	2610	2610
R	0.699	0.658	0.713	0.707	0.794	0.826	0.829	0.821
RMSE	0.238	0.305	0.225	0.223	0.278	0.233	0.269	0.279
MBE	-0.098	0.130	0.041	0.015	-0.135	-0.055	-0.145	-0.158
GCOS	25.6	25.6	27.3	26.5	26.8	34.1	29.0	27.5

- 삭제함: 42
- 삭제함: (all / collocation with GOCI domain)
- 삭제함: N
- 삭제함: 7211 ... [34]
- 삭제함: 7210 ... [35]
- 삭제함: 7210 ... [36]
- 삭제함: 7210 ... [37]
- 삭제함: 4823 ... [38]
- 삭제함: 4823 ... [39]
- 삭제함: 4823 ... [40]
- 삭제함: 4823 ... [41]
- 삭제함: R
- 삭제함: 0.846 ... [42]
- 삭제함: 0.805 ... [43]
- 삭제함: 0.856 ... [44]
- 삭제함: 0.860 ... [45]
- 삭제함: 0.824 ... [46]
- 삭제함: 0.840 ... [47]
- 삭제함: 0.850 ... [48]
- 삭제함: 0.253 ... [49]
- 삭제함: RMSE
- 삭제함: 0.180 ... [50]
- 삭제함: 0.201 ... [51]
- 삭제함: 0.164 ... [52]
- 삭제함: 0.161 ... [53]
- 삭제함: 0.251 ... [54]
- 삭제함: 0.224 ... [55]
- 삭제함: 0.248 ... [56]
- 삭제함: 0.253 ... [57]
- 삭제함: MBE
- 삭제함: -0.066 ... [58]
- 삭제함: 0.051 ... [59]
- 삭제함: 0.018 ... [60]
- 삭제함: 0.017 ... [61]
- 삭제함: -0.103 ... [62]
- 삭제함: -0.044 ... [63]
- 삭제함: -0.124 ... [64]
- 삭제함: -0.134 ... [65]
- 삭제함: %EE
- 삭제함: 53.2 ... [66]
- 삭제함: 58.0 ... [67]
- 삭제함: 63.5 ... [68]
- 삭제함: 65.0 ... [69]
- 삭제함: 51.1 ... [70]
- 삭제함: 56.1 ... [71]
- 삭제함: 52.2 ... [72]
- 삭제함: 50.6 ... [73]



페이지 10: [6] 삭제함	Jhoon Kim	2021. 3. 14. PM 9:30:00
페이지 10: [6] 삭제함	Jhoon Kim	2021. 3. 14. PM 9:30:00
페이지 10: [6] 삭제함	Jhoon Kim	2021. 3. 14. PM 9:30:00
페이지 10: [6] 삭제함	Jhoon Kim	2021. 3. 14. PM 9:30:00
페이지 10: [7] 삭제함	Jhoon Kim	2021. 3. 21. PM 9:44:00
페이지 10: [7] 삭제함	Jhoon Kim	2021. 3. 21. PM 9:44:00
페이지 10: [8] 삭제함	lim	2021. 3. 5. PM 3:51:00
페이지 10: [8] 삭제함	lim	2021. 3. 5. PM 3:51:00
페이지 10: [8] 삭제함	lim	2021. 3. 5. PM 3:51:00
페이지 10: [8] 삭제함	lim	2021. 3. 5. PM 3:51:00
페이지 10: [9] 삭제함	lim	2021. 3. 6. PM 2:21:00
페이지 10: [9] 삭제함	lim	2021. 3. 6. PM 2:21:00
페이지 10: [9] 삭제함	lim	2021. 3. 6. PM 2:21:00
페이지 10: [9] 삭제함	lim	2021. 3. 6. PM 2:21:00
페이지 10: [10] 삭제함	lim	2021. 3. 5. PM 3:54:00
페이지 10: [10] 삭제함	lim	2021. 3. 5. PM 3:54:00

페이지 10: [11] 삭제함 Jhoon Kim 2021. 3. 21. PM 9:54:00

페이지 10: [11] 삭제함 Jhoon Kim 2021. 3. 21. PM 9:54:00

페이지 10: [11] 삭제함 Jhoon Kim 2021. 3. 21. PM 9:54:00

페이지 10: [11] 삭제함 Jhoon Kim 2021. 3. 21. PM 9:54:00

페이지 10: [11] 삭제함 Jhoon Kim 2021. 3. 21. PM 9:54:00

페이지 10: [11] 삭제함 Jhoon Kim 2021. 3. 21. PM 9:54:00

페이지 10: [11] 삭제함 Jhoon Kim 2021. 3. 21. PM 9:54:00

페이지 10: [11] 삭제함 Jhoon Kim 2021. 3. 21. PM 9:54:00

페이지 10: [11] 삭제함 Jhoon Kim 2021. 3. 21. PM 9:54:00

페이지 10: [11] 삭제함 Jhoon Kim 2021. 3. 21. PM 9:54:00

페이지 10: [11] 삭제함 Jhoon Kim 2021. 3. 21. PM 9:54:00

페이지 10: [11] 삭제함 Jhoon Kim 2021. 3. 21. PM 9:54:00

페이지 10: [12] 삭제함 lim 2021. 3. 5. PM 3:51:00

페이지 10: [12] 삭제함 lim 2021. 3. 5. PM 3:51:00

페이지 10: [13] 삭제함 Jhoon Kim 2021. 3. 21. PM 9:58:00

페이지 10: [13] 삭제함 Jhoon Kim 2021. 3. 21. PM 9:58:00

페이지 10: [13] 삭제함 Jhoon Kim 2021. 3. 21. PM 9:58:00

페이지 10: [13] 삭제함 Jhoon Kim 2021. 3. 21. PM 9:58:00

페이지 10: [13] 삭제함 Jhoon Kim 2021. 3. 21. PM 9:58:00

페이지 10: [13] 삭제함 Jhoon Kim 2021. 3. 21. PM 9:58:00

페이지 10: [13] 삭제함 Jhoon Kim 2021. 3. 21. PM 9:58:00

페이지 10: [13] 삭제함 Jhoon Kim 2021. 3. 21. PM 9:58:00

페이지 10: [13] 삭제함 Jhoon Kim 2021. 3. 21. PM 9:58:00

페이지 10: [13] 삭제함 Jhoon Kim 2021. 3. 21. PM 9:58:00

페이지 10: [13] 삭제함 Jhoon Kim 2021. 3. 21. PM 9:58:00

페이지 10: [13] 삭제함 Jhoon Kim 2021. 3. 21. PM 9:58:00

페이지 10: [13] 삭제함 Jhoon Kim 2021. 3. 21. PM 9:58:00

페이지 10: [13] 삭제함 Jhoon Kim 2021. 3. 21. PM 9:58:00

페이지 10: [13] 삭제함 Jhoon Kim 2021. 3. 21. PM 9:58:00

페이지 10: [13] 삭제함 Jhoon Kim 2021. 3. 21. PM 9:58:00

페이지 10: [13] 삭제함 Jhoon Kim 2021. 3. 21. PM 9:58:00

페이지 10: [13] 삭제함 Jhoon Kim 2021. 3. 21. PM 9:58:00

페이지 10: [13] 삭제함 Jhoon Kim 2021. 3. 21. PM 9:58:00

페이지 10: [13] 삭제함 Jhoon Kim 2021. 3. 21. PM 9:58:00

페이지 10: [13] 삭제함 Jhoon Kim 2021. 3. 21. PM 9:58:00

페이지 10: [13] 삭제함 Jhoon Kim 2021. 3. 21. PM 9:58:00

페이지 10: [13] 삭제함 Jhoon Kim 2021. 3. 21. PM 9:58:00

페이지 10: [13] 삭제함 Jhoon Kim 2021. 3. 21. PM 9:58:00

페이지 10: [14] 삭제함 lim 2021. 3. 6. PM 2:46:00

페이지 10: [14] 삭제함 lim 2021. 3. 6. PM 2:46:00

페이지 10: [14] 삭제함 lim 2021. 3. 6. PM 2:46:00

페이지 11: [15] 삭제함 Jhoon Kim 2021. 3. 14. PM 8:13:00

페이지 11: [15] 삭제함 Jhoon Kim 2021. 3. 14. PM 8:13:00

페이지 11: [15] 삭제함 Jhoon Kim 2021. 3. 14. PM 8:13:00

페이지 11: [15] 삭제함 Jhoon Kim 2021. 3. 14. PM 8:13:00

페이지 11: [15] 삭제함 Jhoon Kim 2021. 3. 14. PM 8:13:00

페이지 11: [15] 삭제함 Jhoon Kim 2021. 3. 14. PM 8:13:00

페이지 11: [16] 삭제함 Jhoon Kim 2021. 3. 14. PM 8:17:00

페이지 11: [16] 삭제함 Jhoon Kim 2021. 3. 14. PM 8:17:00

페이지 11: [17] 삭제함 Jhoon Kim 2021. 3. 14. PM 8:21:00

페이지 11: [17] 삭제함 Jhoon Kim 2021. 3. 14. PM 8:21:00

페이지 11: [17] 삭제함	Jhoon Kim	2021. 3. 14. PM 8:21:00
페이지 11: [17] 삭제함	Jhoon Kim	2021. 3. 14. PM 8:21:00
페이지 11: [17] 삭제함	Jhoon Kim	2021. 3. 14. PM 8:21:00
페이지 11: [17] 삭제함	Jhoon Kim	2021. 3. 14. PM 8:21:00
페이지 11: [17] 삭제함	Jhoon Kim	2021. 3. 14. PM 8:21:00
페이지 11: [17] 삭제함	Jhoon Kim	2021. 3. 14. PM 8:21:00
페이지 11: [18] 삭제함	lim	2021. 3. 6. PM 3:20:00
페이지 11: [19] 삭제함	Jhoon Kim	2021. 3. 21. PM 10:07:00
페이지 11: [19] 삭제함	Jhoon Kim	2021. 3. 21. PM 10:07:00
페이지 11: [19] 삭제함	Jhoon Kim	2021. 3. 21. PM 10:07:00
페이지 11: [19] 삭제함	Jhoon Kim	2021. 3. 21. PM 10:07:00
페이지 11: [19] 삭제함	Jhoon Kim	2021. 3. 21. PM 10:07:00
페이지 11: [19] 삭제함	Jhoon Kim	2021. 3. 21. PM 10:07:00
페이지 11: [19] 삭제함	Jhoon Kim	2021. 3. 21. PM 10:07:00
페이지 11: [19] 삭제함	Jhoon Kim	2021. 3. 21. PM 10:07:00
페이지 11: [19] 삭제함	Jhoon Kim	2021. 3. 21. PM 10:07:00
페이지 11: [20] 삭제함	Jhoon Kim	2021. 3. 21. PM 10:10:00
페이지 11: [20] 삭제함	Jhoon Kim	2021. 3. 21. PM 10:10:00



페이지 11: [21] 삭제함	Jhoon Kim	2021. 3. 21. PM 10:15:00
▼		
페이지 11: [21] 삭제함	Jhoon Kim	2021. 3. 21. PM 10:15:00
▼		
페이지 12: [22] 삭제함	Jhoon Kim	2021. 3. 21. PM 10:22:00
▼		
페이지 12: [22] 삭제함	Jhoon Kim	2021. 3. 21. PM 10:22:00
▼		
페이지 12: [22] 삭제함	Jhoon Kim	2021. 3. 21. PM 10:22:00
▼		
페이지 12: [22] 삭제함	Jhoon Kim	2021. 3. 21. PM 10:22:00
▼		
페이지 12: [22] 삭제함	Jhoon Kim	2021. 3. 21. PM 10:22:00
▼		
페이지 12: [22] 삭제함	Jhoon Kim	2021. 3. 21. PM 10:22:00
▼		
페이지 12: [23] 삭제함	Jhoon Kim	2021. 3. 21. PM 10:25:00
▼		
페이지 12: [23] 삭제함	Jhoon Kim	2021. 3. 21. PM 10:25:00
▼		
페이지 12: [24] 서식 지정함 영어(영국)	lim	2021. 3. 28. PM 2:42:00
▲		
페이지 12: [24] 서식 지정함 영어(영국)	lim	2021. 3. 28. PM 2:42:00
▲		
페이지 12: [24] 서식 지정함 영어(영국)	lim	2021. 3. 28. PM 2:42:00
▲		
페이지 12: [25] 삭제함	Jhoon Kim	2021. 3. 14. PM 8:27:00
▼		
페이지 12: [25] 삭제함	Jhoon Kim	2021. 3. 14. PM 8:27:00
▼		
페이지 12: [25] 삭제함	Jhoon Kim	2021. 3. 14. PM 8:27:00
▼		

페이지 12: [25] 삭제함 Jhoon Kim 2021. 3. 14. PM 8:27:00

▼ ▲  
페이지 12: [25] 삭제함 Jhoon Kim 2021. 3. 14. PM 8:27:00

▼ ▲  
페이지 12: [25] 삭제함 Jhoon Kim 2021. 3. 14. PM 8:27:00

▼ ▲  
페이지 12: [25] 삭제함 Jhoon Kim 2021. 3. 14. PM 8:27:00

▼ ▲  
페이지 12: [25] 삭제함 Jhoon Kim 2021. 3. 14. PM 8:27:00

▼ ▲  
페이지 12: [25] 삭제함 Jhoon Kim 2021. 3. 14. PM 8:27:00

▼ ▲  
페이지 12: [25] 삭제함 Jhoon Kim 2021. 3. 14. PM 8:27:00

▼ ▲  
페이지 12: [25] 삭제함 Jhoon Kim 2021. 3. 14. PM 8:27:00

▼ ▲  
페이지 12: [25] 삭제함 Jhoon Kim 2021. 3. 14. PM 8:27:00

▼ ▲  
페이지 12: [25] 삭제함 Jhoon Kim 2021. 3. 14. PM 8:27:00

▼ ▲  
페이지 12: [25] 삭제함 Jhoon Kim 2021. 3. 14. PM 8:27:00

▼ ▲  
페이지 12: [25] 삭제함 Jhoon Kim 2021. 3. 14. PM 8:27:00

▼ ▲  
페이지 12: [25] 삭제함 Jhoon Kim 2021. 3. 14. PM 8:27:00

▼ ▲  
페이지 12: [25] 삭제함 Jhoon Kim 2021. 3. 14. PM 8:27:00

▼ ▲  
페이지 12: [25] 삭제함 Jhoon Kim 2021. 3. 14. PM 8:27:00

▼ ▲  
페이지 12: [25] 삭제함 Jhoon Kim 2021. 3. 14. PM 8:27:00

▼ ▲  
페이지 12: [25] 삭제함 Jhoon Kim 2021. 3. 14. PM 8:27:00

▼ ▲  
페이지 12: [25] 삭제함 Jhoon Kim 2021. 3. 14. PM 8:27:00

페이지 12: [25] 삭제함	Jhoon Kim	2021. 3. 14. PM 8:27:00
▼	▶	
페이지 12: [25] 삭제함	Jhoon Kim	2021. 3. 14. PM 8:27:00
▼	▶	
페이지 12: [25] 삭제함	Jhoon Kim	2021. 3. 14. PM 8:27:00
▼	▶	
페이지 12: [25] 삭제함	Jhoon Kim	2021. 3. 14. PM 8:27:00
▼	▶	
페이지 12: [25] 삭제함	Jhoon Kim	2021. 3. 14. PM 8:27:00
▼	▶	
페이지 12: [25] 삭제함	Jhoon Kim	2021. 3. 14. PM 8:27:00
▼	▶	
페이지 12: [25] 삭제함	Jhoon Kim	2021. 3. 14. PM 8:27:00
▼	▶	
페이지 12: [25] 삭제함	Jhoon Kim	2021. 3. 14. PM 8:27:00
▼	▶	
페이지 12: [25] 삭제함	Jhoon Kim	2021. 3. 14. PM 8:27:00
▼	▶	
페이지 12: [25] 삭제함	Jhoon Kim	2021. 3. 14. PM 8:27:00
▼	▶	
페이지 12: [26] 삭제함	Jhoon Kim	2021. 3. 28. AM 10:27:00
▼	▶	
페이지 12: [26] 삭제함	Jhoon Kim	2021. 3. 28. AM 10:27:00
▼	▶	
페이지 12: [26] 삭제함	Jhoon Kim	2021. 3. 28. AM 10:27:00
▼	▶	
페이지 12: [26] 삭제함	Jhoon Kim	2021. 3. 28. AM 10:27:00
▼	▶	
페이지 13: [27] 삭제함	Jhoon Kim	2021. 3. 28. AM 10:32:00
▼	▶	
페이지 13: [27] 삭제함	Jhoon Kim	2021. 3. 28. AM 10:32:00
▼	▶	
페이지 13: [27] 삭제함	Jhoon Kim	2021. 3. 28. AM 10:32:00
▼	▶	



페이지 13: [30] 삭제함 Jhoon Kim 2021. 3. 28. AM 11:11:00

▼  
페이지 13: [30] 삭제함 Jhoon Kim 2021. 3. 28. AM 11:11:00

▼  
페이지 13: [30] 삭제함 Jhoon Kim 2021. 3. 28. AM 11:11:00

▼  
페이지 13: [30] 삭제함 Jhoon Kim 2021. 3. 28. AM 11:11:00

▼  
페이지 13: [30] 삭제함 Jhoon Kim 2021. 3. 28. AM 11:11:00

▼  
페이지 13: [30] 삭제함 Jhoon Kim 2021. 3. 28. AM 11:11:00

▼  
페이지 13: [30] 삭제함 Jhoon Kim 2021. 3. 28. AM 11:11:00

▼  
페이지 13: [30] 삭제함 Jhoon Kim 2021. 3. 28. AM 11:11:00

▼  
페이지 13: [30] 삭제함 Jhoon Kim 2021. 3. 28. AM 11:11:00

▼  
페이지 13: [30] 삭제함 Jhoon Kim 2021. 3. 28. AM 11:11:00

▼  
페이지 13: [30] 삭제함 Jhoon Kim 2021. 3. 28. AM 11:11:00

▼  
페이지 13: [30] 삭제함 Jhoon Kim 2021. 3. 28. AM 11:11:00

▼  
페이지 13: [30] 삭제함 Jhoon Kim 2021. 3. 28. AM 11:11:00

▼  
페이지 13: [30] 삭제함 Jhoon Kim 2021. 3. 28. AM 11:11:00

▼  
페이지 13: [30] 삭제함 Jhoon Kim 2021. 3. 28. AM 11:11:00

▼  
페이지 13: [30] 삭제함 Jhoon Kim 2021. 3. 28. AM 11:11:00

▼  
페이지 13: [30] 삭제함 Jhoon Kim 2021. 3. 28. AM 11:11:00

▼  
▼

페이지 13: [30] 삭제함 Jhoon Kim 2021. 3. 28. AM 11:11:00

▼

페이지 13: [30] 삭제함 Jhoon Kim 2021. 3. 28. AM 11:11:00

▼

페이지 13: [30] 삭제함 Jhoon Kim 2021. 3. 28. AM 11:11:00

▼

페이지 13: [30] 삭제함 Jhoon Kim 2021. 3. 28. AM 11:11:00

▼

페이지 13: [30] 삭제함 Jhoon Kim 2021. 3. 28. AM 11:11:00

▼

페이지 13: [30] 삭제함 Jhoon Kim 2021. 3. 28. AM 11:11:00

▼

페이지 13: [31] 삭제함 Jhoon Kim 2021. 3. 28. AM 11:37:00

▼

페이지 13: [31] 삭제함 Jhoon Kim 2021. 3. 28. AM 11:37:00

▼

페이지 13: [31] 삭제함 Jhoon Kim 2021. 3. 28. AM 11:37:00

▼

페이지 13: [31] 삭제함 Jhoon Kim 2021. 3. 28. AM 11:37:00

▼

페이지 13: [31] 삭제함 Jhoon Kim 2021. 3. 28. AM 11:37:00

▼

페이지 13: [31] 삭제함 Jhoon Kim 2021. 3. 28. AM 11:37:00

▼

페이지 13: [31] 삭제함 Jhoon Kim 2021. 3. 28. AM 11:37:00

▼

페이지 13: [31] 삭제함 Jhoon Kim 2021. 3. 28. AM 11:37:00

▼

페이지 13: [31] 삭제함 Jhoon Kim 2021. 3. 28. AM 11:37:00

▼

페이지 13: [31] 삭제함 Jhoon Kim 2021. 3. 28. AM 11:37:00

▼

페이지 13: [31] 삭제함 Jhoon Kim 2021. 3. 28. AM 11:37:00

▼

페이지 13: [31] 삭제함 Jhoon Kim 2021. 3. 28. AM 11:37:00

페이지 13: [31] 삭제함	Jhoon Kim	2021. 3. 28. AM 11:37:00
▼		
페이지 13: [31] 삭제함	Jhoon Kim	2021. 3. 28. AM 11:37:00
▼		
페이지 13: [32] 삭제함	Jhoon Kim	2021. 3. 28. AM 11:53:00
▼		
페이지 13: [32] 삭제함	Jhoon Kim	2021. 3. 28. AM 11:53:00
▼		
페이지 13: [32] 삭제함	Jhoon Kim	2021. 3. 28. AM 11:53:00
▼		
페이지 13: [32] 삭제함	Jhoon Kim	2021. 3. 28. AM 11:53:00
▼		
페이지 13: [32] 삭제함	Jhoon Kim	2021. 3. 28. AM 11:53:00
▼		
페이지 13: [32] 삭제함	Jhoon Kim	2021. 3. 28. AM 11:53:00
▼		
페이지 13: [32] 삭제함	Jhoon Kim	2021. 3. 28. AM 11:53:00
▼		
페이지 13: [32] 삭제함	Jhoon Kim	2021. 3. 28. AM 11:53:00
▼		
페이지 13: [32] 삭제함	Jhoon Kim	2021. 3. 28. AM 11:53:00
▼		
페이지 13: [32] 삭제함	Jhoon Kim	2021. 3. 28. AM 11:53:00
▼		
페이지 21: [33] 삭제함	lim	2021. 2. 25. PM 4:09:00
▼		
페이지 41: [34] 삭제함	lim	2021. 3. 5. AM 9:13:00
▼		
페이지 41: [35] 삭제함	lim	2021. 3. 5. AM 9:13:00
▼		
페이지 41: [36] 삭제함	lim	2021. 3. 5. AM 9:13:00

페이지 41: [37] 삭제함	lim	2021. 3. 5. AM 9:13:00
페이지 41: [38] 삭제함	lim	2021. 3. 5. AM 9:13:00
페이지 41: [39] 삭제함	lim	2021. 3. 5. AM 9:13:00
페이지 41: [40] 삭제함	lim	2021. 3. 5. AM 9:13:00
페이지 41: [41] 삭제함	lim	2021. 3. 5. AM 9:13:00
페이지 41: [42] 삭제함	lim	2021. 3. 5. AM 9:13:00
페이지 41: [43] 삭제함	lim	2021. 3. 5. AM 9:13:00
페이지 41: [44] 삭제함	lim	2021. 3. 5. AM 9:13:00
페이지 41: [45] 삭제함	lim	2021. 3. 5. AM 9:13:00
페이지 41: [46] 삭제함	lim	2021. 3. 5. AM 9:13:00
페이지 41: [47] 삭제함	lim	2021. 3. 5. AM 9:13:00
페이지 41: [48] 삭제함	lim	2021. 3. 5. AM 9:13:00
페이지 41: [49] 삭제함	lim	2021. 3. 5. AM 9:13:00
페이지 41: [50] 삭제함	lim	2021. 3. 5. AM 9:13:00
페이지 41: [51] 삭제함	lim	2021. 3. 5. AM 9:13:00
페이지 41: [52] 삭제함	lim	2021. 3. 5. AM 9:13:00
페이지 41: [53] 삭제함	lim	2021. 3. 5. AM 9:13:00
페이지 41: [54] 삭제함	lim	2021. 3. 5. AM 9:13:00

페이지 41: [55] 삭제함 lim 2021. 3. 5. AM 9:13:00

페이지 41: [56] 삭제함 lim 2021. 3. 5. AM 9:13:00

페이지 41: [57] 삭제함 lim 2021. 3. 5. AM 9:13:00

페이지 41: [58] 삭제함 lim 2021. 3. 5. AM 9:13:00

페이지 41: [59] 삭제함 lim 2021. 3. 5. AM 9:13:00

페이지 41: [60] 삭제함 lim 2021. 3. 5. AM 9:13:00

페이지 41: [61] 삭제함 lim 2021. 3. 5. AM 9:13:00

페이지 41: [62] 삭제함 lim 2021. 3. 5. AM 9:13:00

페이지 41: [63] 삭제함 lim 2021. 3. 5. AM 9:13:00

페이지 41: [64] 삭제함 lim 2021. 3. 5. AM 9:13:00

페이지 41: [65] 삭제함 lim 2021. 3. 5. AM 9:13:00

페이지 41: [66] 삭제함 lim 2021. 3. 5. AM 9:13:00

페이지 41: [67] 삭제함 lim 2021. 3. 5. AM 9:13:00

페이지 41: [68] 삭제함 lim 2021. 3. 5. AM 9:13:00

페이지 41: [69] 삭제함 lim 2021. 3. 5. AM 9:13:00

페이지 41: [70] 삭제함 lim 2021. 3. 5. AM 9:13:00

페이지 41: [71] 삭제함 lim 2021. 3. 5. AM 9:13:00

페이지 41: [72] 삭제함 lim 2021. 3. 5. AM 9:13:00

